Supporting Information for

Unravelling the Mechanism of Excited-State Interligand Energy Transfer and the Engineering of Dual Emission in $[Ir(C^N)_2(N^N)]^+$ Complexes

Paul A. Scattergood,*[a,b] Anna M. Ranieri,[d] Luke Charalambou,[a] Adrian Comia,[a] Daniel A.W. Ross,[a]

Craig R. Rice,[a] Samantha J.O. Hardman,[e] Jean-Louis Heully,[c] Isabelle M. Dixon,[c] Massimiliano Massi,[d]

Fabienne Alary*[c] and Paul I.P. Elliott*[a,b]

a Department of Chemistry, University of Huddersfield, Huddersfield, HD1 3DH, UK

b Centre for Functional Materials, University of Huddersfield, Huddersfield, HD1 3DH, UK

c Laboratoire de Chimie et Physique Quantiques, UMR 5626 CNRS/Université Toulouse 3 - Paul Sabatier, Université de Toulouse, 118 route de Narbonne, Toulouse, 31062, France

d School of Molecular and Life Sciences – Curtin Institute for Functional Materials and Interfaces, Curtin University, Building 500, Kent Street, Bentley, Western Australia, Australia

e Manchester Institute of Biotechnology, The University of Manchester, 131 Princess Street, Manchester, M1 7DN, UK

Contents

Experimental methods and synthetic procedures		**S4-S11**
Figure S1	^{1}H NMR spectrum of pymtz ligand in $CDCl_3$	**S12**
Figure S2	^{13}C NMR spectrum of pymtz ligand in $CDCl_3$	**S13**
Figure S3	^{1}H NMR spectrum of pyztz ligand in $CDCl_3$	**S14**
Figure S4	^{13}C NMR spectrum of pyztz ligand in $CDCl_3$	**S15**
Figure S5	^{1}H NMR spectrum of **1b** in d^3-MeCN	**S16**
Figure S6	^{13}C NMR spectrum of **1b** in d^3-MeCN	**S17**
Figure S7	High resolution ESI mass spectrum for **1b**	**S18**
Figure S8	^{1}H NMR spectrum of **1c** in d^3-MeCN	**S19**
Figure S9	^{13}C NMR spectrum of **1c** in d^3-MeCN	**S20**
Figure S10	High resolution ESI mass spectrum for **1c**	**S21**
Figure S11	^{1}H NMR spectrum of **2b** in d^3-MeCN	**S22**
Figure S12	^{13}C NMR spectrum of **2b** in d^3-MeCN	**S23**
Figure S13	High resolution ESI mass spectrum for **2b**	**S24**
Figure S14	^{1}H NMR spectrum of **2c** in d^3-MeCN	**S25**
Figure S15	^{13}C NMR spectrum of **2c** in d^3-MeCN	**S26**
Figure S16	High resolution ESI mass spectrum for **2c**	**S27**
Figure S17	^{1}H NMR spectrum of **3a** in d^3-MeCN	**S28**
Figure S18	^{13}C NMR spectrum of **3a** in d^3-MeCN	**S29**
Figure S19	High resolution ESI mass spectrum for **3a**	**S30**
Figure S20	^{1}H NMR spectrum of **3b** in d^3-MeCN	**S31**
Figure S21	^{13}C NMR spectrum of **3b** in d^3-MeCN	**S32**
Figure S22	High resolution ESI mass spectrum for **3b**	**S33**
Figure S23	^{1}H NMR spectrum of **3c** in d^3-MeCN	**S34**
Figure S24	^{13}C NMR spectrum of **3c** in d^3-MeCN	**S35**
Figure S25	High resolution ESI mass spectrum for **3c**	**S36**
Summarised crystallographic data for **pymtz**, **2b** and **2c**		**S37**
Figure S26	Molecular structure of ligand **pymtz**	**S38**
Figure S27	Photoluminescence excitation spectra for **1b**	**S38**
Figure S28	Variable wavelength photoluminescence lifetime data for **1b**	**S39**
Remark – Solvent-dependant dual emission of **1b**		**S39**
Table S1	Variable temperature photoluminescence lifetimes for **1a**-**2c**	**S40**
Transient absorption spectroscopy experimental information		**S41**

Figure S29 Transient absorption spectra for **2a-2c** **S41**
Table S2 Summarised TA kinetic time constants for **1a-1c** and **2a-2c** **S42**
Computational methods and details **S42**
Figure S30 Molecular orbital energies and isosurface plots for **2a-2c** **S43**
Figure S31 Molecular orbital energies and isosurface plots for **3a-3c** **S44**
Figure S32 Spin density plots for calculated ^{3}MLCT/^{3}LC and ^{3}MLCT/^{3}LL'CT states of **1a-3c** **S44**
Figure S33 Spin density plots for calculated one-electron oxidised and reduced forms of **1a-3c** **S47**
Figure S34 TD-DFT calculated UV-Visible absorption spectra for **1a-3c** **S50**
Figure S35 Vibrationally resolved emission spectra calculated for ^{3}MLCT/^{3}LC and ^{3}MLCT/^{3}LL'CT states of **1a-3c** at 77 K and 300 K **S51**
Theoretical analysis of the vibronic emission spectra of compound **1a** **S52**
Figure S36 Step by step procedure for the identification of effective frequencies for **1a** **S53**
Figure S37 Adimensional displacements and their associated frequencies for **1a** **S54**
Figure S38 Representation of the atomic displacements involved in the modes responsible for the multi-peak emission spectrum of ^{3}MLCT/^{3}LC of **1a** **S55**
Theoretical analysis of the vibrational resolved emission spectrum of the ^{3}MLCT/^{3}LL'CT state of compound **1b** **S56**
Figure S39 Adimensional displacements, DDNC and VRES for **1b** **S56**
Figure S40 Representation of the atomic displacements involved in the modes responsible for the emission spectrum of ^{3}MLCT/^{3}LL'CT of **1b** **S57**
Figure S41 Calculated dipole moments for **1a**, **1b**, **2c** **S57**
Figure S42 Spin density plots and NEB calculation determined MEP for **1b** **S58**
Figure S43 Spin density plots and NEB calculation determined MEP for **2c** **S58**
Figure S44 Calculated transition state modes for **1a** and **1b** **S59**
Figure S45 Evolution of selected bond lengths for **1b** along MEP **S59**
References **S60**

General Methods

$[\{Ir(ppy)_2Cl\}_2]$,[1] $[\{Ir(dfppy)_2Cl\}_2]$,[2] pytz[3] **1a**[4] and **2a**[5] were prepared according to previously reported procedures. **Caution:** *care should be taken in the preparation of triazole-containing compounds utilising organic azide starting materials as these precursors are potentially explosive.* Minimal C atom to N atom ratios of at least 2.5:1 to 3:1 are recommended to mitigate this risk if the organic azide is to be isolated prior to use rather than prepared and used *in situ.* All reagents were purchased from Acros Organics, Alfa Aesar, Sigma-Aldrich and Fluorochem and used as received. Synthetic manipulations requiring an inert atmosphere were performed under dry N_2 using standard Schlenk line techniques. Deaeration of solvents was performed through vigorous bubbling with N_2 for a period of at least 15 minutes. NMR spectra were recorded on Bruker Ascend 400 MHz and 500 MHz spectrometers, with all chemical shifts being reported in ppm, calibrated relative to the residual solvent signal ($CHCl_3$, ^{1}H: δ 7.26, ^{13}C: δ 77.16; MeCN, ^{1}H: δ 1.94, ^{13}C: δ 1.32, 118.26). High resolution mass spectrometry was performed on an Agilent 6210 TOF instrument with a dual ESI source.

UV-Visible electronic absorption spectra were recorded on an Agilent Cary-60 spectrophotometer utilising quartz cells of 1 cm pathlength. Emission spectra were recorded on a Fluoromax-4 spectrophotometer utilising 1 cm pathlength quartz cells. 'Degassed' solutions were prepared via three repeat freeze-pump-thaw cycles. Photoluminescence quantum yields are quoted relative to $[Ru(bpy)_3][PF_6]_2$ in aerated MeCN, with all complexes being excited at a single wavelength with common optical density. Quantum yields are thus determined from the ratio of integrated areas under the relevant emission profiles, with an assumed experimental uncertainty of ±10%. Luminescence lifetimes were determined using an Edinburgh Instruments Mini-τ equipped with a picosecond diode laser (404 nm, 56 ps) excitation source.

Cyclic voltammograms were measured using a PalmSens EmStat3 potentiostat with PSTrace electrochemical software (version 4.8). Analyte solutions (typical concentration 1.65 $mmoldm^{-3}$) were prepared using N_2 saturated MeCN, freshly distilled from CaH_2. All measurements were performed under an atmosphere of N_2 at scan rates ranging from 50 to 500 mVs^{-1}. NBu_4PF_6 was employed as supporting electrolyte, being recrystallised from EtOH and oven dried prior to use, with a typical solution concentration of 0.2 $moldm^{-3}$. The working electrode was glassy carbon, the counter electrode Pt wire and the reference Ag/AgCl, the latter being chemically isolated from the analyte solution by an electrolyte-containing bridge tube tipped with a porous frit. Ferrocence was employed as an internal reference, with all potentials being reported relative to the Fc^+/Fc couple.

Synthesis of 2-(trimethylsilylethynyl)pyrimidine

2-Bromopyrimidine (1.51 g, 9.50 mmol), $Pd(PPh_3)_2Cl_2$ (0.34 g, 0.48 mmol, 5 mol%) and CuI (0.18 g, 0.95 mmol, 10 mol%) were added to previously deaerated 2:1 (v/v) dry THF/Et_3N (60 ml). Ethynyltrimethylsilane (3.4 ml, 24.5 mmol) was added and the dark brown coloured solution stirred at 50 ^oC for 17 h under N_2. After cooling to room temperature the reaction mixture was passed through a short silica pad. The filtrate was concentrated under reduced pressure and then purified *via* column chromatography (SiO_2, CH_2Cl_2), with the product being obtained initially as a yellow oil and then as a brown coloured solid after thorough drying *in vacuo*. Yield = 1.39 g, 83 %. ^1H NMR ($CDCl_3$, 400 MHz): 0.29 (s, 9H), 7.23 (t, J = 4.9 Hz, 1H), 8.70 (d, J = 4.9 Hz, 2H). ^{13}C NMR ($CDCl_3$, 101 MHz): -0.35, 94.63, 102.39, 120.17, 152.71, 157.37. HRMS (ES); m/z calc. for $C_9H_{13}N_2Si$: 177.0843, found: 177.0845 (MH^+).

Synthesis of 2-(1-benzyl-1,2,3-triazol-4-yl)pyrimidine (pymtz)

Benzyl azide (0.64 g, 4.80 mmol) and 2-(trimethylsilylethynyl)pyrimidine (0.76 g, 4.31 mmol) were added to a mixed solvent system of THF (25 ml), H_2O (25 ml) and ^{t}BuOH (5 ml). To this mixture were added, in order, $CuSO_4.5H_2O$ (0.28 g, 1.12 mmol), sodium ascorbate (0.43 g, 2.17 mmol), K_2CO_3 (0.90 g, 6.50 mmol) and excess pyridine (5 ml). The resulting reaction mixture was stirred at room temperature for 18 h before removal of the organic solvents under reduced pressure. $CHCl_3$ (90 ml) and conc. aq. NH_3 (5 ml) were added to the aqueous suspension, with the resulting biphasic mixture being stirred vigorously at room temperature for a further 1 h. The organic layer was separated and the aqueous phase extracted with a further portion (50 mL) of $CHCl_3$. The combined organic phases were washed successively with dilute aq. NH_3 (3 x 100 ml), H_2O (100 ml) and brine (100 ml) before being dried over $MgSO_4$. The volume of the solvent was reduced to a minimum with the addition of excess hexane precipitating the pure product from solution as a beige-coloured powder. Yield = 0.74 g, 72 %. ^1H NMR ($CDCl_3$, 400 MHz): 5.59 (s, 2H), 7.18 (t, J = 4.9 Hz, 1H), 7.28-7.40 (m, 5H), 8.13 (s, 1H), 8.75 (d, J = 4.9 Hz, 2H). ^{13}C NMR ($CDCl_3$, 101 MHz): 54.49, 119.74, 124.81, 128.38, 129.01, 129.30, 134.26, 147.68, 157.60, 159.15. HRMS (ES); m/z calc. for $C_{13}H_{12}N_5$: 238.1087, found: 238.1089 (MH^+); m/z calc. for $C_{13}H_{11}N_5Na$: 260.0907, found: 260.0910 ($M+Na^+$); m/z calc. for $C_{26}H_{22}N_{10}Na$: 497.1927, found: 497.1919 ($2M+Na^+$).

Synthesis of 2-(trimethylsilylethynyl)pyrazine

To previously deaerated 2:1 (v/v) dry THF/Et_3N (60 ml) were added $Pd(PPh_3)_2Cl_2$ (0.10 g, 0.14 mmol, 5 mol%), CuI (0.06 g, 0.31 mmol, 10 mol%), 2-iodopyrazine (0.30 ml, 3.04 mmol) followed by ethynyltrimethylsilane (1.03 ml, 7.44 mmol). The reaction mixture was stirred at 50 ^oC for 19 h under N_2 then cooled to room temperature and passed through a short silica pad. The filtrate was concentrated under reduced pressure then purified *via* column chromatography (SiO_2, CH_2Cl_2), with the product obtained as a yellow oil. Yield = 0.42 g, 79 %. ^1H NMR ($CDCl_3$, 400 MHz): 0.28 (s, 9H), 8.47 (d, *J* = 2.5 Hz, 1H), 8.51-8.54 (m, 1H), 8.67 (d, *J* = 1.3 Hz, 1H). ^{13}C NMR ($CDCl_3$, 101 MHz): -0.40, 99.81, 100.67, 139.92, 143.09, 144.36, 147.92. HRMS (ES); m/z calc. for $C_9H_{13}N_2Si$: 177.0843, found: 177.0843 (MH^+).

Synthesis of 2-(1-benzyl-1,2,3-triazol-4-yl)pyrazine (pyztz)

Benzyl azide (0.19 g, 1.42 mmol) and 2-(trimethylsilylethynyl)pyrazine (0.23 g, 1.30 mmol) were added to a mixed solvent system of THF (25 ml), H_2O (25 ml) and ^{t}BuOH (5 ml). To this mixture were added in order $CuSO_4.5H_2O$ (0.08 g, 0.32 mmol), sodium ascorbate (0.11 g, 0.55 mmol), K_2CO_3 (0.27 g, 1.96 mmol) and excess pyridine (5 ml). The reaction mixture was stirred at room temperature for 22 h before removal of the organic solvents under reduced pressure. $CHCl_3$ (90 ml) and conc. aq. NH_3 (5 ml) were added to the aqueous suspension which was then stirred vigorously for a further hour at room temperature. The organic layer was removed and the aqueous phase extracted with a further portion (50 ml) of $CHCl_3$. The combined organic phases were washed successively with dilute aq. NH_3 (2 x 100 ml), H_2O (100 ml) and brine (2 x 100 ml) before being dried over $MgSO_4$. The solvent was evaporated to dryness with the residue subsequently dissolved in the minimum volume of CH_2Cl_2. Addition of excess hexane precipitated the pure product from solution as an off-white powder. Yield = 0.19 g, 63 %. ^1H NMR ($CDCl_3$, 400 MHz): 5.59 (s, 2H), 7.29-7.42 (m, 5H), 8.06 (s, 1H), 8.45-8.50 (m, 2H), 9.40 (d, *J* = 1.0 Hz, 1H). ^{13}C NMR ($CDCl_3$, 101 MHz): 54.58, 122.99, 128.40, 129.10, 129.36, 134.20, 142.26, 143.74, 143.99, 145.98, 146.39. HRMS (ES); m/z calc. for $C_{13}H_{12}N_5$: 238.1087, found: 238.1089 (MH^+); m/z calc. for $C_{13}H_{11}N_5Na$: 260.0907, found: 260.0913 ($M+Na^+$); m/z calc. for $C_{26}H_{22}N_{10}Na$: 497.1927, found: 497.1919 ($2M+Na^+$).

Synthesis of [Ir(ppy)$_2$(pymtz)][PF$_6$] (1b)

2-(1-Benzyl-1,2,3-triazol-4-yl)pyrimidine (85 mg, 0.36 mmol), [{Ir(ppy)$_2$Cl}$_2$] (193 mg, 0.18 mmol) and excess NH_4PF_6 (217 mg, 1.33 mmol) were added to deaerated 1:1 (v/v) $CHCl_3$ / MeOH (35 ml) and heated to 60 ^oC under N_2 for 16 h. The bright yellow coloured solution was allowed to cool to room temperature, with excess Et_2O then added to ensure complete precipitation of the product. The solids were collected by filtration and washed with a small portion of H_2O (10 ml) followed by Et_2O. Purification was achieved *via* column chromatography (SiO_2, 9:1 CH_2Cl_2 / MeCN) with additional recrystallisation from CH_2Cl_2 / hexane affording the product as a yellow solid. Yield = 167 mg, 53 %. ^{1}H NMR (CD_3CN, 400 MHz): 5.61 (s, 2H), 6.21-6.28 (m, 2H), 6.82 (td, *J* = 1.3, 7.4 Hz, 1H), 6.88-6.97 (m, 2H), 7.01-7.13 (m, 3H), 7.19-7.25 (m, 2H), 7.33-7.42 (m, 4H), 7.70-7.80 (m, 4H), 7.87 (tt, *J* = 1.3, 7.9 Hz, 2H), 7.98 (dd, *J* = 2.2, 5.6 Hz, 1H), 8.02-8.07 (m, 2H), 8.74 (s, 1H), 8.93 (dd, *J* = 2.1 Hz, 4.9 Hz, 1H). ^{13}C NMR (CD_3CN, 101 MHz): 56.38, 120.56, 120.80, 123.27, 123.59, 123.82, 124.27, 124.65, 125.30, 125.76, 129.00, 129.43, 129.90, 130.01, 130.60, 131.25, 132.35, 132.60, 134.52, 139.54, 139.66, 145.13, 145.18, 146.45, 147.71, 148.59, 150.54, 150.85, 158.14, 160.43, 160.68, 167.86, 168.25. HRMS (ES); m/z calc. for $C_{35}H_{27}N_7Ir$: 738.1952, found: 738.1963 (M^+). Anal. Calc'd for $C_{35}H_{27}N_7IrPF_6$ (%): C 47.62, H 3.08, N 11.11, found (%): C 47.49, H 2.97, N 10.90.

Synthesis of [Ir(ppy)$_2$(pyztz)][PF$_6$] (1c)

2-(1-Benzyl-1,2,3-triazol-4-yl)pyrazine (89 mg, 0.38 mmol), [{Ir(ppy)$_2$Cl}$_2$] (203 mg, 0.19 mmol) and excess NH_4PF_6 (203 mg, 1.25 mmol) were added to deaerated 1:1 (v/v) $CHCl_3$ / MeOH (35 ml) and heated to 60 ^oC under N_2 for 16 h. After cooling of the red coloured solution to room temperature excess Et_2O was added to ensure complete precipitation of the product. The solids were collected by filtration and washed with a small portion of H_2O (10 ml) followed by Et_2O. Purification was achieved *via* column chromatography (SiO_2, 4:1 CH_2Cl_2 / MeCN) with additional recrystallisation form CH_2Cl_2 / hexane affording the product as a pale orange solid. Yield = 198 mg, 59%. ^{1}H NMR (CD_3CN, 400 MHz): 5.60 (d, *J* = 15.0 Hz, 1H), 5.64 (d, *J* = 15.0 Hz, 1H), 6.22 (dd, *J* = 0.7, 7.7 Hz, 1H), 6.26 (dd, *J* = 0.7, 7.6 Hz, 1H), 6.84 (td, *J* = 1.3, 7.5 Hz, 1H), 6.90-7.00 (m, 2H), 7.00-7.12 (m, 3H), 7.23-7.29 (m, 2H), 7.37-7.45 (m, 3H), 7.63 (d, *J* = 5.8 Hz, 1H), 7.69-7.82 (m, 4H), 7.88 (t, *J* = 7.8 Hz, 2H), 8.03-8.08 (m, 2H), 8.53 (d, *J* = 3.0 Hz, 1H),

8.69 (s, 1H), 9.30 (s, 1H). ^{13}C NMR (CD_3CN, 101 MHz): 56.42, 120.61, 120.85, 123.38, 123.91, 124.29, 124.63, 125.32, 125.76, 127.48, 129.33, 130.04, 130.09, 130.65, 131.28, 132.34, 132.51, 134.23, 139.60, 139.72, 144.75, 145.03, 145.17, 145.64, 146.82, 147.24, 148.75, 148.78, 150.49, 150.84, 167.84, 168.13. HRMS (ES); m/z calc. for $C_{35}H_{27}N_7Ir$: 738.1952, found: 738.1966 (M^+).

Synthesis of [Ir(dfppy)$_2$(pymtz)][PF$_6$] (2b)

2-(1-Benzyl-1,2,3-triazol-4-yl)pyrimidine (91 mg, 0.38 mmol), [{Ir(dfppy)$_2$Cl}$_2$] (230 mg, 0.19 mmol) and NH_4PF_6 (151 mg, 0.93 mmol) were added to deaerated 1:1 (v/v) $CHCl_3$ / MeOH (30 ml) and heated to 45 ^{o}C under N_2 in the dark for 19 h. The orange coloured solution was cooled to room temperature then reduced in volume, with the addition of excess hexane giving a precipitate which was collected by filtration and washed with H_2O (5 ml) followed by Et_2O. Purification was achieved *via* column chromatography (SiO_2, 1% MeOH / CH_2Cl_2) with additional recrystallisation from CH_2Cl_2 / hexane giving the product as a very pale yellow solid. Yield = 201 mg, 55 %. ^{1}H NMR (CD_3CN, 400 MHz): 5.63 (s, 2H), 5.68 (dd, *J* = 2.3, 8.7 Hz, 1H), 5.76 (dd, *J* = 2.3, 8.7 Hz, 1H), 6.61 (ddd, *J* = 2.3, 9.5, 13.0 Hz, 1H), 6.70 (ddd, *J* = 2.3, 9.5, 13.0 Hz, 1H), 7.10 (ddd, *J* = 1.2, 6.0, 7.5 Hz, 1H), 7.16 (ddd, *J* = 1.2, 6.0, 7.5 Hz, 1H), 7.19-7.26 (m , 2H), 7.32-7.39 (m, 3H), 7.43 (t, *J* = 5.5 Hz, 1H), 7.75-7.80 (m, 2H), 7.88-7.96 (m, 2H), 8.07 (dd, *J* = 2.1, 5.6 Hz, 1H), 8.24-8.34 (m, 2H), 8.76 (s, 1H), 8.97 (dd, *J* = 2.1, 4.9 Hz, 1H). ^{13}C NMR (CD_3CN, 151 MHz): 56.65, 99.56 (t, *J* = 27.3 Hz), 100.08 (t, *J* = 27.3 Hz), 114.79 (dd, *J* = 2.8, 15.9 Hz), 114.90 (dd, *J* = 2.8, 15.9 Hz), 123.81, 124.35, 124.48, 124.64, 124.78, 125.15, 129.12 (m), 129.16, 129.23 (m), 129.66, 130.01, 130.06, 134.37, 140.61, 140.68, 147.58, 150.41 (d, *J* = 7.0 Hz), 151.00, 151.24, 152.59 (d, *J* = 6.4 Hz), 158.73, 160.40, 160.99, 161.67 (dd, *J* = 12.9, 260.6 Hz), 162.15 (dd, *J* = 12.5, 260.1 Hz), 163.70 (dd, *J* = 12.1, 255.7 Hz), 164.26 (d, *J* = 7.1 Hz), 164.30 (dd, *J* = 12.4, 255.7 Hz), 164.5 (d, *J* = 7.1 Hz). HRMS (ES); m/z calc. for $C_{35}H_{23}N_7F_4Ir$: 810.1575, found: 810.1584 (M^+). Anal. Calc'd for $C_{35}H_{23}N_7IrPF_{10}$ (%): C 44.03, H 2.43, N 10.27, found (%): C 43.87, H 2.33, N 10.24.

Synthesis of [Ir(dfppy)$_2$(pyztz)][PF$_6$] (2c)

2-(1-Benzyl-1,2,3-triazol-4-yl)pyrazine (93 mg, 0.39 mmol), [{Ir(dfppy)$_2$Cl}$_2$] (237 mg, 0.20 mmol) and NH_4PF_6 (153 mg, 0.94 mmol) were added to deaerated 1:1 (v/v) $CHCl_3$ / MeOH (20 ml) and heated to 45 ^oC under N_2 in the dark for 19 h. The yellow coloured suspension was allowed to cool to room temperature, with excess hexane then added to ensure complete precipitation of the product. The solids were collected by filtration, being washed with a small portion of H_2O (5 ml) followed by Et_2O. Purification was achieved *via* column chromatography (SiO_2, 2% MeOH / CH_2Cl_2) with additional recrystallisation from CH_2Cl_2 / hexane giving the product as a bright yellow powder. Yield = 216 mg, 58 %. ^{1}H NMR (CD_3CN, 400 MHz): 5.61 (d, *J* = 14.9 Hz, 1H), 5.65 (d, *J* = 15.0 Hz, 1H), 5.68 (dd, *J* = 2.2, 8.8 Hz, 1H), 5.76 (dd, *J* = 2.3, 8.6 Hz, 1H), 6.63 (ddd, *J* = 2.3, 9.7, 12.8 Hz, 1H), 6.72 (ddd, *J* = 2.3, 9.7, 12.9 Hz, 1H), 7.08 (ddd, *J* = 1.2, 5.8, 7.3 Hz, 1H), 7.15 (ddd, *J* = 1.1, 5.7, 7.3 Hz, 1H), 7.24-7.30 (m, 2H), 7.37-7.43 (m, 3H), 7.65 (d, *J* = 5.7 Hz, 1H), 7.73 (d, *J* = 5.5 Hz, 1H), 7.84-7.88 (m, 1H), 7.90-7.97 (m, 2H), 8.30 (t, *J* = 8.5 Hz, 2H), 8.58 (d, *J* = 2.9 Hz, 1H), 8.70 (s, 1H), 9.33 (d, *J* = 1.1 Hz, 1H). ^{13}C NMR (CD_3CN, 151 MHz): 56.66, 99.62 (t, *J* = 27.1 Hz), 100.15 (t, *J* = 27.0 Hz), 114.71 (dd, *J* = 2.8, 18.3 Hz), 114.87 (dd, *J* = 2.8, 18.2 Hz), 124.36, 124.49, 124.65, 124.78, 125.11, 127.77, 129.09 (dd, *J* = 2.8, 5.0 Hz), 129.16 (*J* = 2.8, 5.0 Hz), 129.45, 130.12, 134.08, 140.63, 140.72, 145.14, 145.22, 145.43, 147.16, 149.12, 150.72 (d, *J* = 6.9 Hz), 150.94, 151.21, 152.74 (d, *J* = 6.9 Hz), 161.67 (dd, *J* = 12.8, 260.0 Hz), 162.13 (dd, *J* = 12.8, 260.0 Hz), 163.69 (dd, *J* = 12.4, 255.2 Hz), 164.23 (d, *J* = 6.6 Hz), 164.30 (dd, *J* = 12.4, 255.9 Hz), 164.39 (d, *J* = 6.9 Hz). HRMS (ES); m/z calc. for $C_{35}H_{23}N_7F_4Ir$: 810.1575, found: 810.1566 (M^+). Anal. Calc'd for $C_{35}H_{23}N_7IrPF_{10}$ (%): C 44.03, H 2.43, N 10.27, found (%): C 44.14, H 2.35, N 10.26.

Synthesis of [{Ir(ptz)$_2$Cl}$_2$]

A 3:1 (v/v) mixture of 2-ethoxyethanol / H_2O (26 ml) was heated to 50 ^oC and vigorously sparged with N_2 for a period of 15 minutes, after which 2-(1-Benzyl-1,2,3-triazol-4-yl)benzene[6] (488 mg, 2.07 mmol) and $IrCl_3$. xH_2O (380 mg, 1.05 mmol based on 53 wt% Ir) were added. The reaction mixture was heated to 125 ^oC under N_2 for 21 hours and then cooled to room temperature. The bright yellow precipitated solids were

collected by filtration, washed with H_2O followed by Et_2O and dried *in vacuo*. The product (yield = 698 mg, 96 %) was used in subsequent synthetic steps without further purification or characterisation.

Synthesis of [Ir(ptz)$_2$(pytz)][PF$_6$] (3a)

2-(1-Benzyl-1,2,3-triazol-4-yl)pyridine (52 mg, 0.22 mmol), [{Ir(ptz)$_2$Cl}$_2$] (149 mg, 0.11 mmol) and excess NH_4PF_6 (108 mg, 0.66 mmol) were added to deaearted 1:1 (v/v) $CHCl_3$ / MeOH (25 ml) and stirred under N_2 at 50 ^oC in the dark for 16 hours. The solution was allowed to cool to room temperature then hexane added to afford an off-white coloured precipitate. The solids were collected by filtration, being washed with H_2O (10 ml) followed by Et_2O. Purification was achieved *via* column chromatography (SiO_2, 9:1 CH_2Cl_2 / MeCN), with further recrystallisation from CH_2Cl_2 / hexane giving the title complex as a very pale yellow solid. Yield = 142 mg, 62 %. ^{1}H NMR (CD_3CN, 400 MHz): 5.40-5.50 (m, 4H), 5.51 (d, *J* = 15.3 Hz, 1H), 5.56 (d, *J* = 15.2 Hz, 1H), 6.16-6.24 (m, 2H), 6.70 (td, *J* = 0.9, 7.4 Hz, 1H), 6.77-6.85 (m, 2H), 6.93 (t, *J* = 7.4 Hz, 1H), 7.14-7.30 (m, 7H), 7.30-7.43 (m, 10H), 7.46 (d, *J* = 7.2 Hz, 1H), 7.89-8.00 (m, 3H), 8.06 (s, 1H), 8.07 (s, 1H), 8.54 (s, 1H). ^{13}C NMR (CD_3CN, 101 MHz): 56.02, 56.09, 56.15, 120.64, 120.80, 122.88, 122.99, 123.27, 123.37, 123.73, 126.11, 126.75, 128.44, 128.80, 129.15, 129.72, 129.85, 129.95, 130.04, 133.09, 133.89, 134.87, 135.32, 135.37, 136.72, 136.82, 140.26, 142.92, 145.89, 150.40, 150.87, 151.74, 157.70, 158.17. HRMS (ES); m/z calc. for $C_{44}H_{36}N_{10}Ir$: 897.2748, found: 897.2746 (M^+). Anal. Calc'd for $C_{44}H_{36}N_{10}IrPF_6$ (%): C 50.72, H 3.48, N 13.44, found (%): C 50.58, H 3.40, N 13.47.

Synthesis of [Ir(ptz)$_2$(pymtz)][PF$_6$] (3b)

2-(1-Benzyl-1,2,3-triazol-4-yl)pyrimidine (89 mg, 0.38 mmol), [{Ir(ptz)$_2$Cl}$_2$] (260 mg, 0.19 mmol) and excess NH_4PF_6 (153 mg, 0.94 mmol) were added to deaerated 1:1 (v/v) $CHCl_3$ / MeOH (25 ml) and stirred under N_2 in the dark at 50 ^oC for 19 hours. The solvent was removed by rotary evaporation with the resulting residue being redissolved in the minimum volume of CH_2Cl_2. Addition of hexane afforded a pale yellow precipitate which was collected by filtration, washed with H_2O (5 ml) followed by Et_2O and dried *in vacuo*. Purification was achieved *via* column chromatography (SiO_2, 2% MeOH / CH_2Cl_2), with further recrystallisation from CH_2Cl_2 / hexane affording the product as a pale yellow coloured powder. Yield = 213 mg, 54 %.

^{1}H NMR (CD_3CN, 400 MHz): 5.42-5.53 (m, 4H), 5.58 (d, *J* = 15.4 Hz, 1H), 5.63 (d, *J* = 15.3 Hz, 1H), 6.14-6.21 (m, 2H), 6.72 (td, *J* = 1.2, 7.4 Hz, 1H), 6.81 (td, *J* = 1.2, 7.4 Hz, 1H), 6.86 (td, *J* = 0.8, 7.4 Hz, 1H), 6.95 (td, *J* = 0.8, 7.4 Hz, 1H), 7.16-7.30 (m, 6H), 7.30-7.44 (m, 11H), 7.47 (dd, *J* = 0.7, 7.5 Hz, 1H), 8.09 (s, br. 2H), 8.13 (dd, *J* = 2.1, 5.6 Hz, 1H), 8.71 (s, 1H), 8.88 (dd, *J* = 2.1, 5.0 Hz, 1H). ^{13}C NMR (101 MHz, CD_3CN): 56.15, 56.22, 120.73, 120.88, 122.81, 123.08, 123.44, 123.48, 124.00, 128.51, 128.62, 128.64, 128.89, 128.98, 129.21, 129.74, 129.77, 129.82, 129.96, 129.98, 130.02, 133.08, 133.78, 134.95, 135.25, 135.29, 136.70, 136.75, 142.02, 144.17, 148.25, 157.57, 157.94, 158.71, 160.14, 161.25. HRMS (ES); m/z calc. for $C_{43}H_{35}N_{11}Ir$: 898.2701, found: 898.2701 (M^+). Anal. Calc'd for $C_{43}H_{35}N_{11}IrPF_6$ (%): C 49.52, H 3.38, N 14.77, found (%): C 49.36, H 3.27, N 14.70.

Synthesis of $[Ir(ptz)_2(pyztz)][PF_6]$ (3c)

2-(1-Benzyl-1,2,3-triazol-4-yl)pyrazine (97 mg, 0.41 mmol), $[\{Ir(ptz)_2Cl\}_2]$ (283 mg, 0.20 mmol) and excess NH_4PF_6 (164 mg, 1.00 mmol) were added to deaerated 1:1 (v/v) $CHCl_3$ / MeOH (25 ml) and stirred under N_2 at 50 ^{o}C in the dark for 19 hours. The reaction mixture was allowed to cool to room temperature, with addition of excess hexane ensuring complete precipitation of the orange coloured product. The solids were collected by filtration, being washed with H_2O (5 ml) followed by Et_2O then dried *in vacuo*. Purification was achieved *via* column chromatography (SiO_2, 2% MeOH / CH_2Cl_2), with further recrystallisation from CH_2Cl_2 / hexane affording the title complex as a pale orange solid. Yield = 227 mg, 53 %. ^{1}H NMR (CD_3CN, 400 MHz): 5.41-5.51 (m, 4H), 5.58 (d, *J* = 14.9 Hz, 1H), 5.63 (d, *J* = 14.9 Hz, 1H), 6.14-6.20 (m, 2H), 6.73 (td, *J* = 1.0, 7.5 Hz, 1H), 6.82 (td, *J* = 1.0, 7.5 Hz, 1H), 6.87 (t, *J* = 7.4 Hz, 1H), 6.97 (t, *J* = 7.3 Hz, 1H), 7.20-7.29 (m, 6H), 7.33-7.41 (m, 9H), 7.43 (d, *J* = 7.4 Hz, 1H), 7.48 (d, *J* = 7.4 Hz, 1H), 7.93-7.97 (m, 1H), 8.08 (s, 1H), 8.09 (s, 1H), 8.50 (d, *J* = 3.0 Hz, 1H), 8.68 (s, 1H), 9.25 (d, *J* = 0.9 Hz, 1H). ^{13}C NMR (CD_3CN, 101 MHz): 56.15, 56.22, 120.77, 120.92, 123.12, 123.45, 123.58, 124.10, 126.67, 128.58, 128.90, 128.95, 129.24, 129.74, 129.77, 129.95, 129.96, 130.08, 133.07, 133.66, 134.66, 135.21, 135.25, 136.55, 136.73, 142.32, 144.28, 144.30, 145.46, 146.40, 147.79, 148.00, 157.61, 157.86. HRMS (ES); m/z calc. for $C_{43}H_{35}N_{11}Ir$: 898.2701, found: 898.2700 (M^+). Anal. Calc'd for $C_{43}H_{35}N_{11}IrPF_6$ (%): C 49.52, H 3.38, N 14.77, found (%): C 49.06, H 3.00, N 14.66.

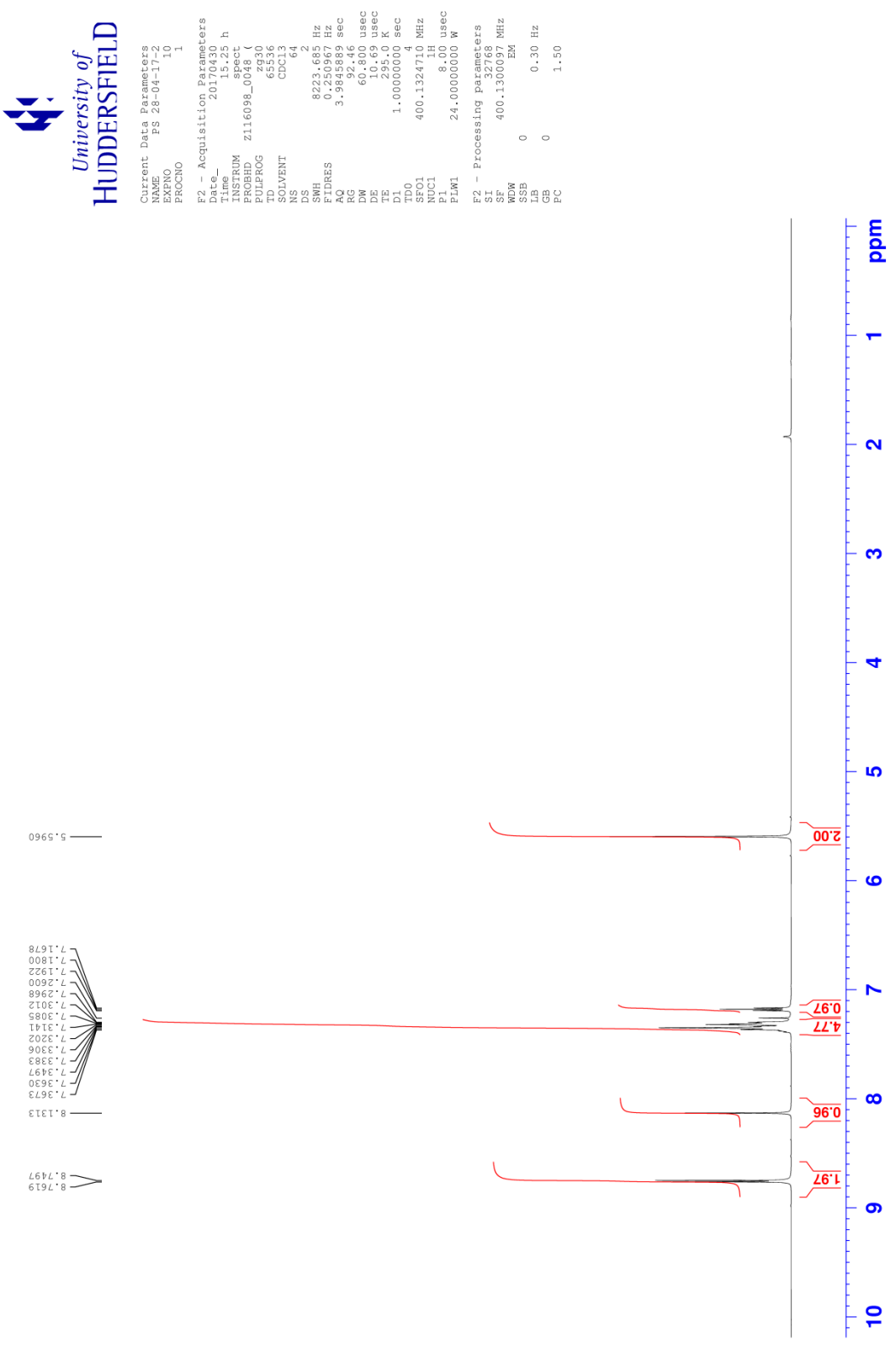

Figure S1 ^{1}H NMR (400 MHz, $CDCl_3$) spectrum of 2-(1-benzyl-1,2,3-triazol-4-yl)pyrimidine (pymtz)

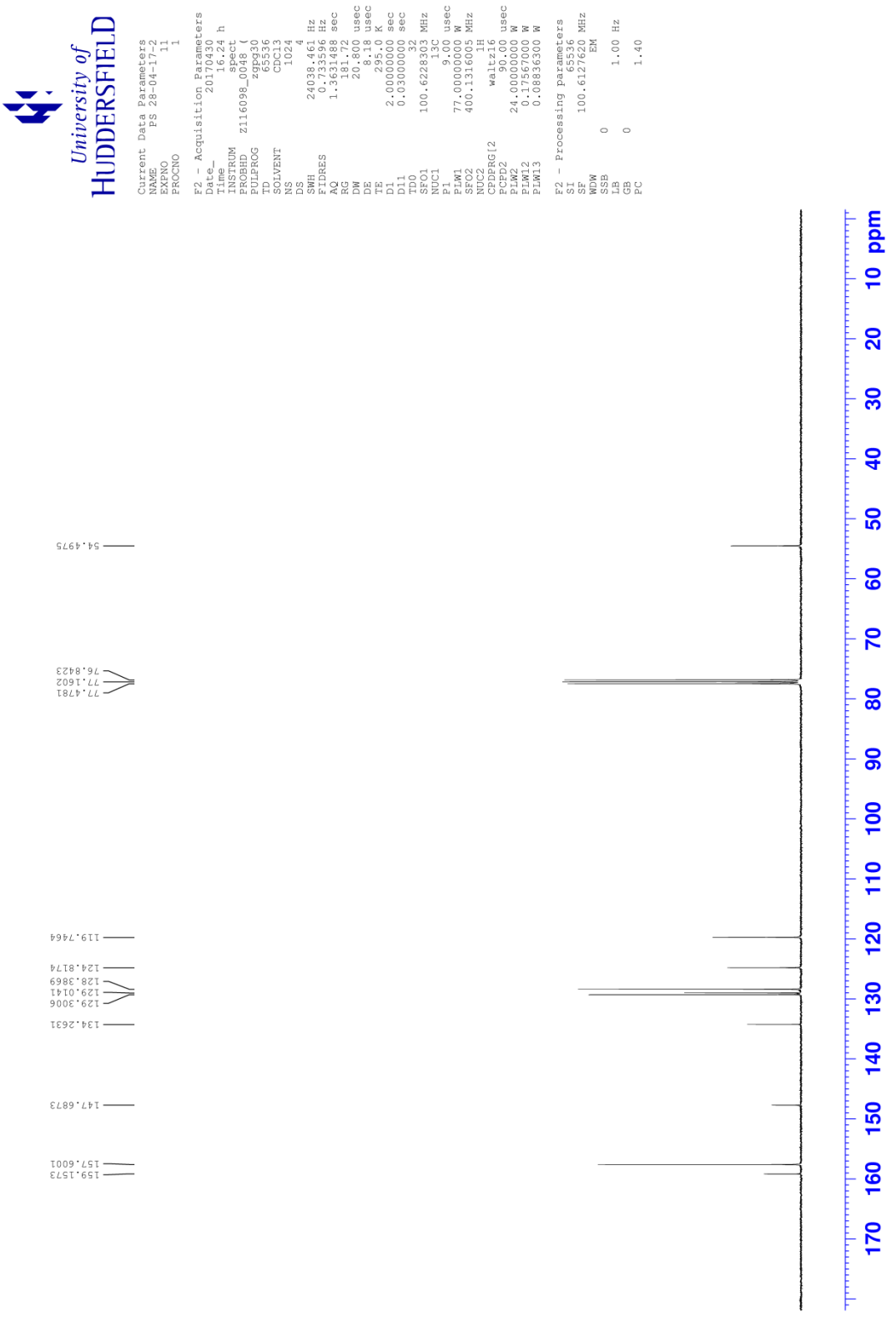

Figure S2 ^{13}C NMR (101 MHz, $CDCl_3$) spectrum of 2-(1-benzyl-1,2,3-triazol-4-yl)pyrimidine (pymtz)

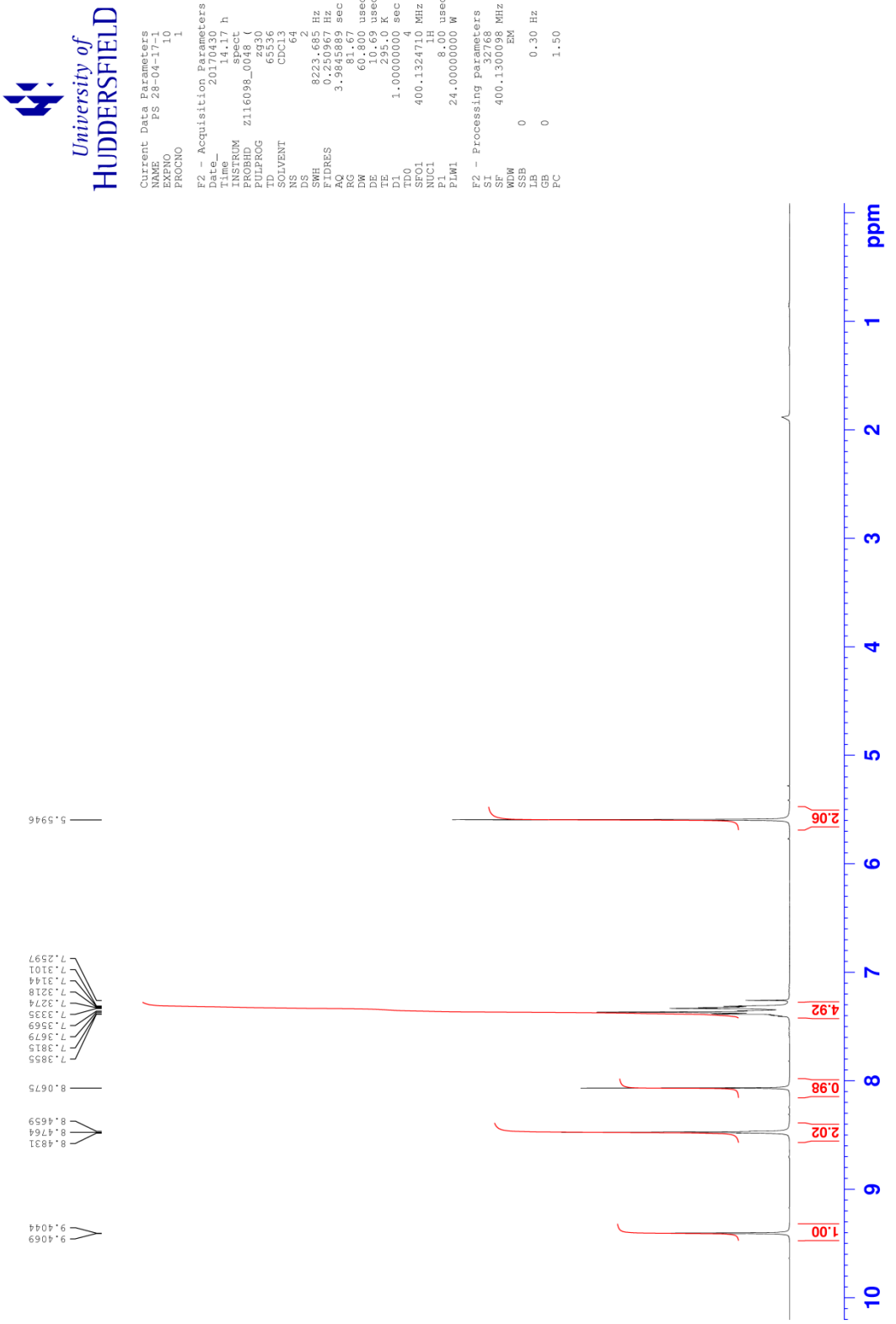

Figure S3 ^{1}H NMR (400 MHz, $CDCl_3$) spectrum of 2-(1-benzyl-1,2,3-triazol-4-yl)pyrazine (pyztz)

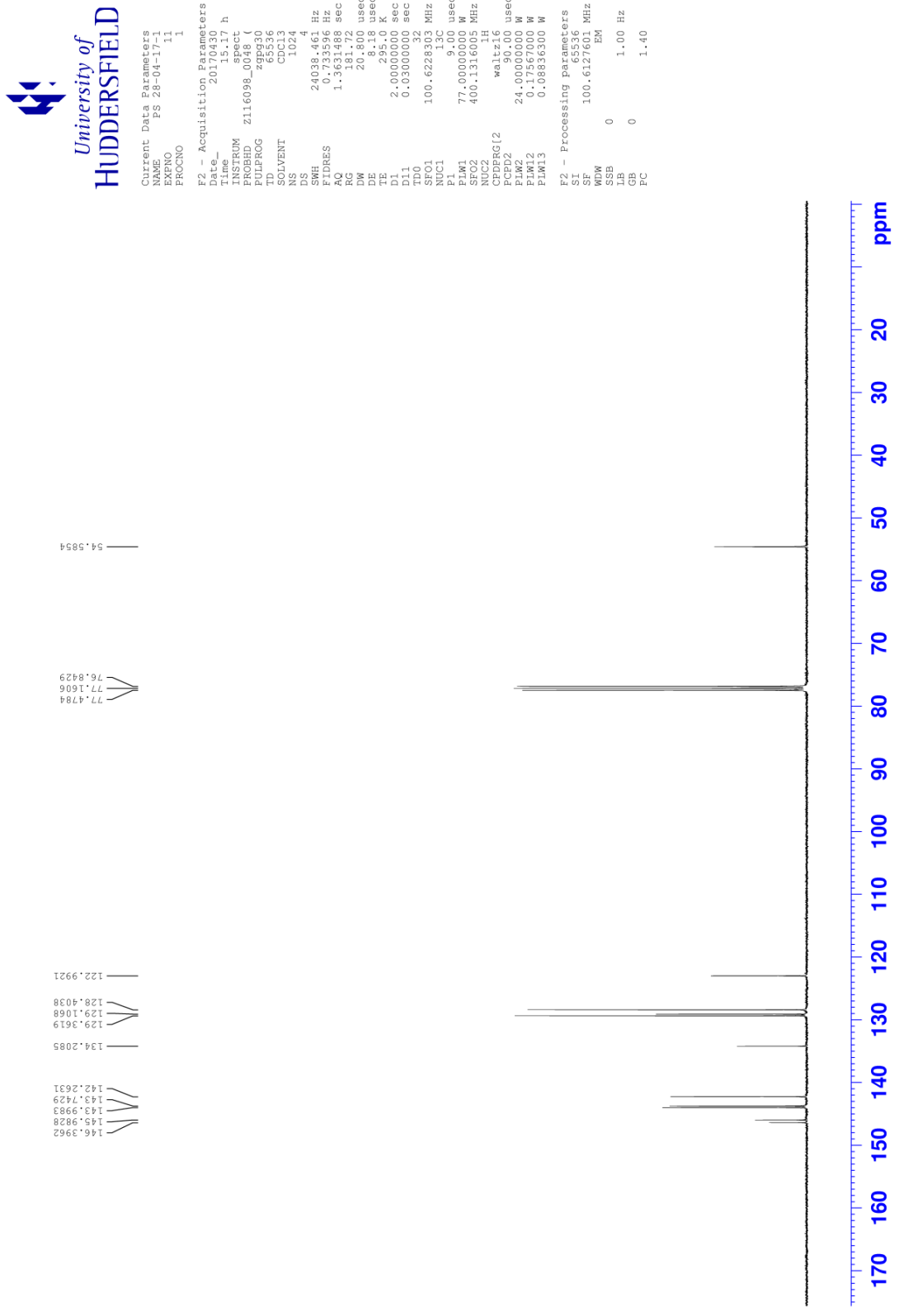

Figure S4 ^{13}C NMR (101 MHz, $CDCl_3$) spectrum of 2-(1-benzyl-1,2,3-triazol-4-yl)pyrazine (pyztz)

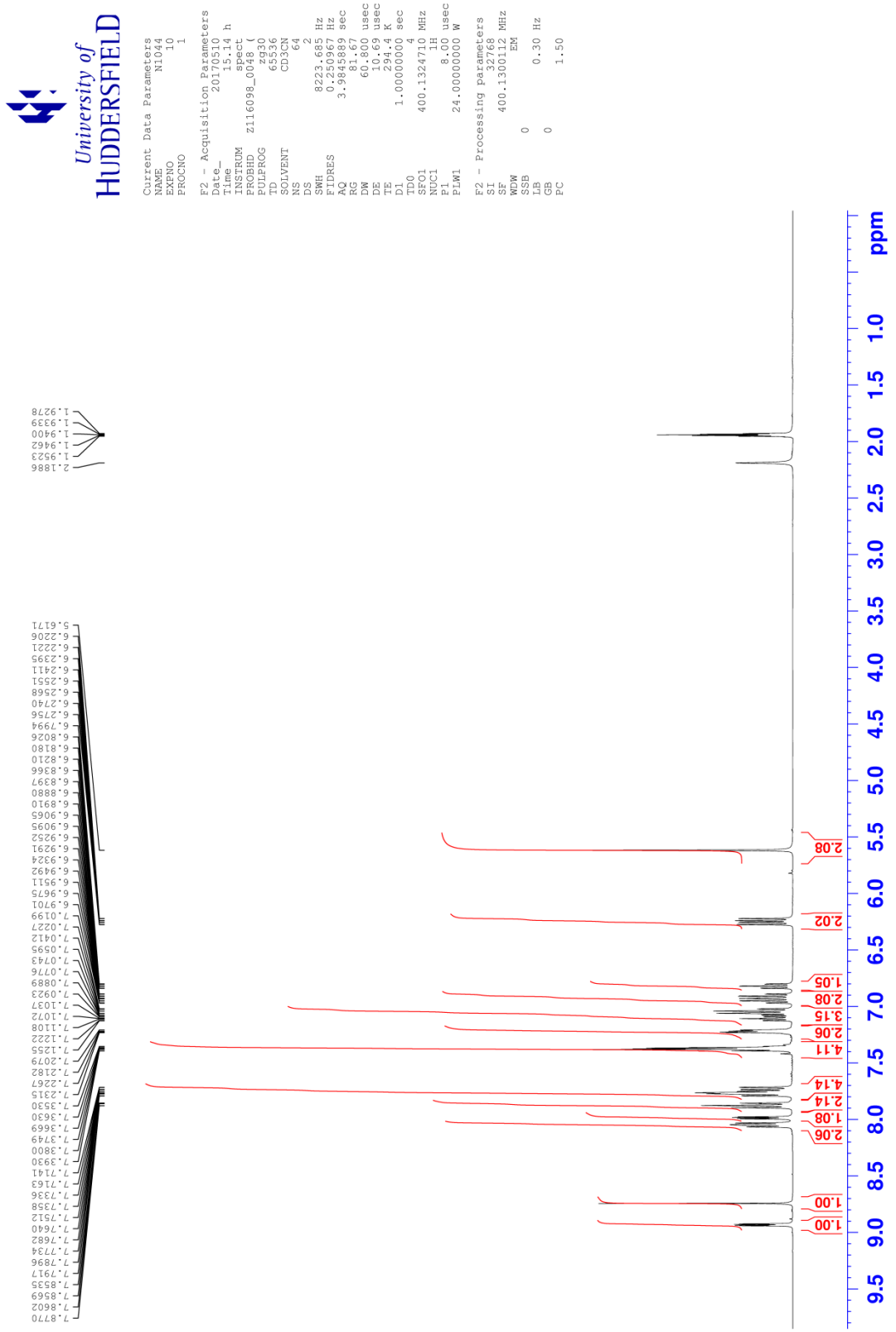

Figure S5 ^{1}H NMR (400 MHz, d_3-MeCN) spectrum of $[(ppy)_2Ir(pymtz)][PF_6]$ (**1b**)

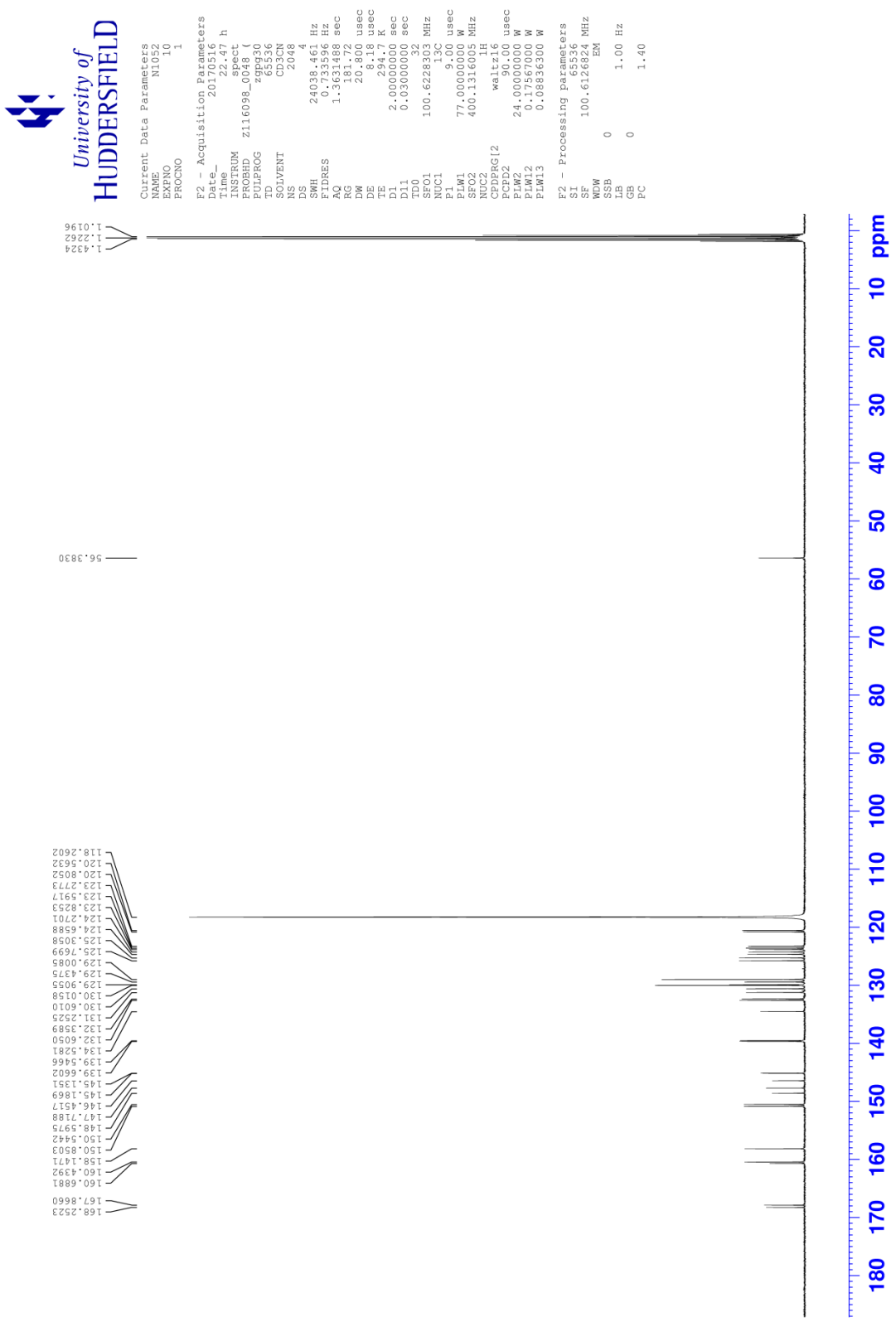

Figure S6 ^{13}C NMR (101 MHz, d_3-MeCN) spectrum of $[(ppy)_2Ir(pymtz)][PF_6]$ (**1b**)

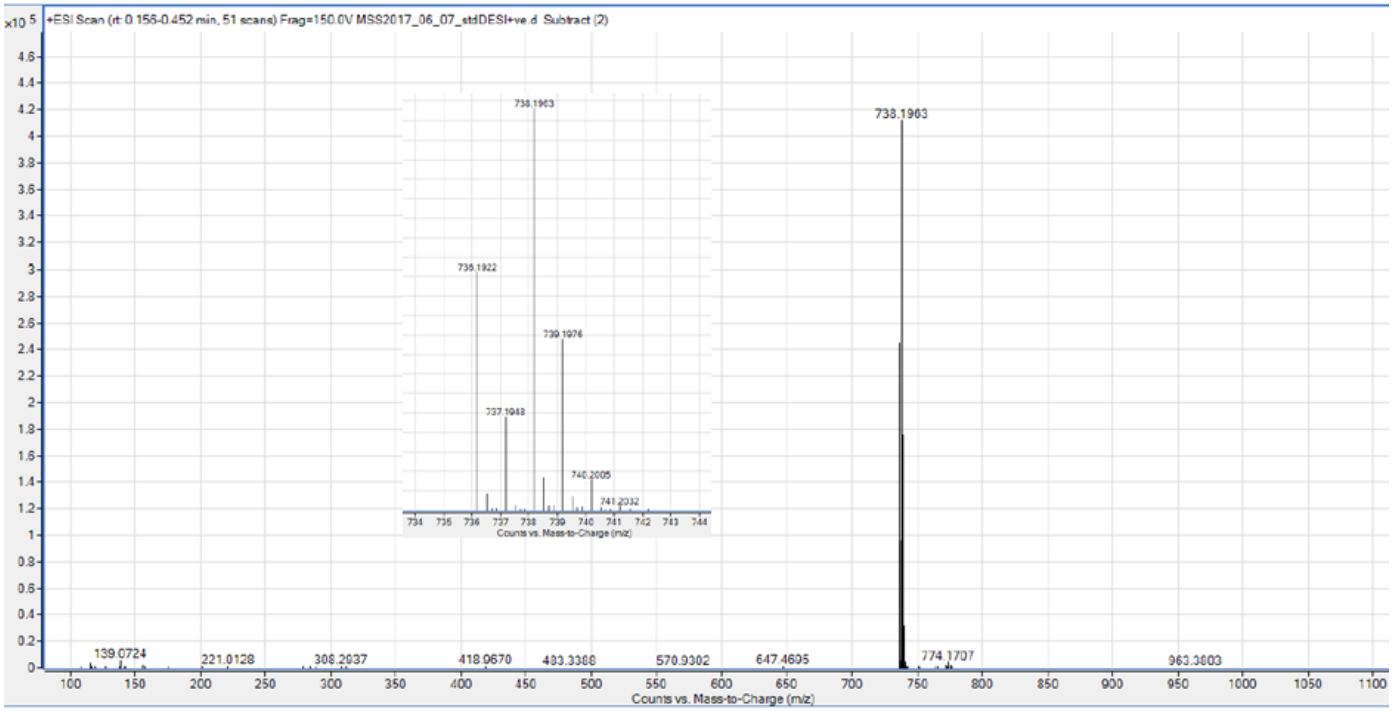

Figure S7 High resolution ESI mass spectrum of $[(ppy)_2Ir(pymtz)][PF_6]$ (**1b**). The expansion shows detail of the cationic $[C_{35}H_{27}N_7Ir]^+$ mass fragment.

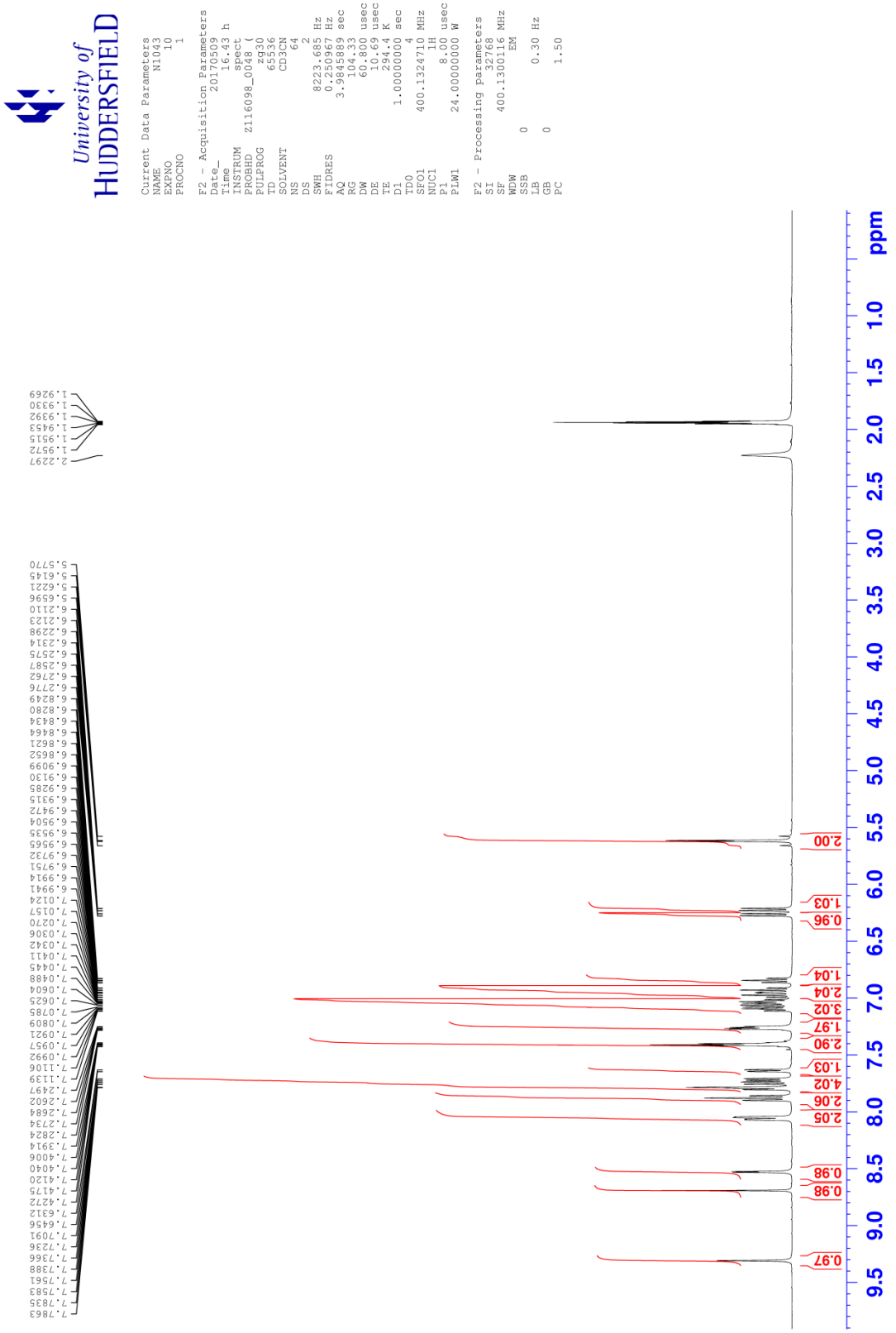

Figure S8 ^{1}H NMR (400 MHz, d_3-MeCN) spectrum of $[(ppy)_2Ir(pyztz)][PF_6]$ (**1c**)

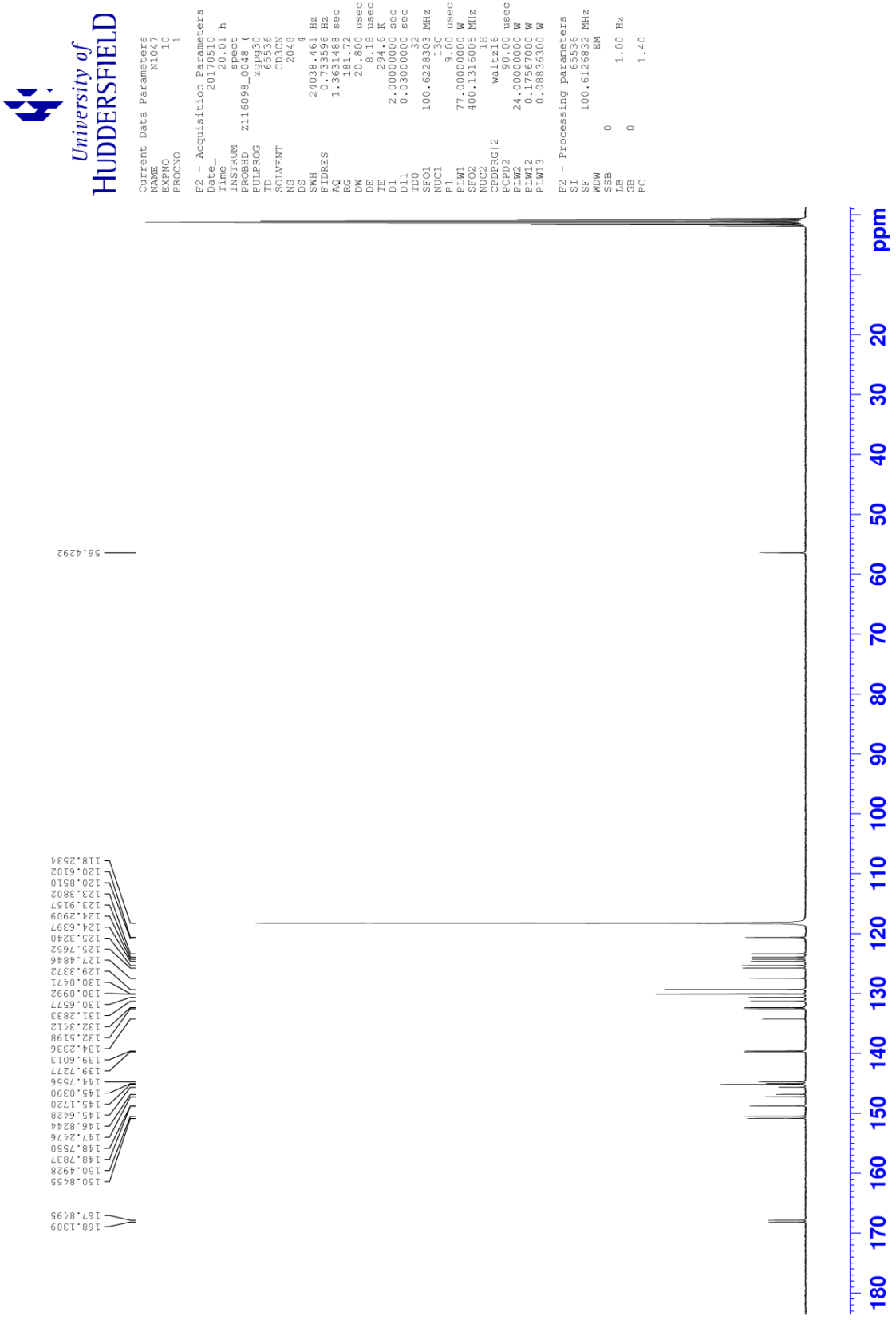

Figure S9 ^{13}C NMR (101 MHz, d_3-MeCN) spectrum of $[(ppy)_2Ir(pyztz)][PF_6]$ (**1c**)

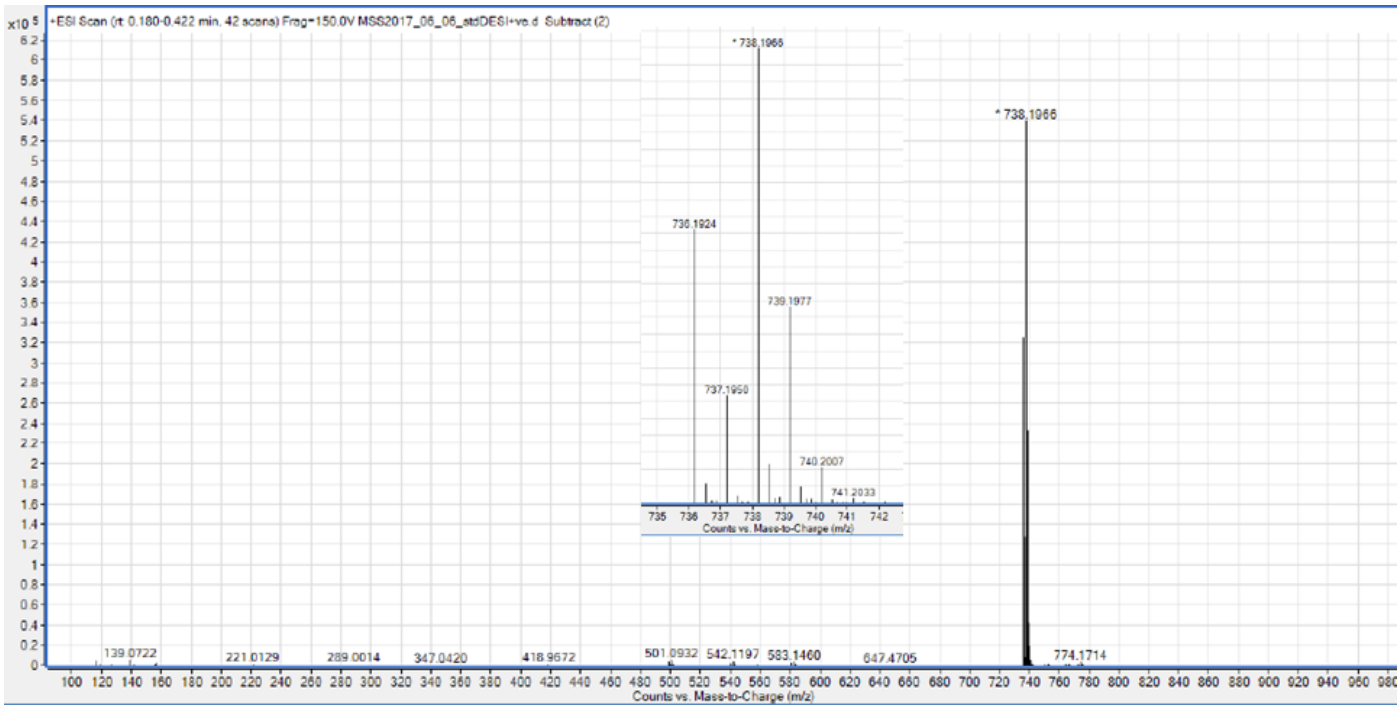

Figure S10 High resolution ESI mass spectrum of $[(ppy)_2Ir(pyztz)][PF_6]$ (**1c**). The expansion shows detail of the cationic $[C_{35}H_{27}N_7Ir]^+$ mass fragment.

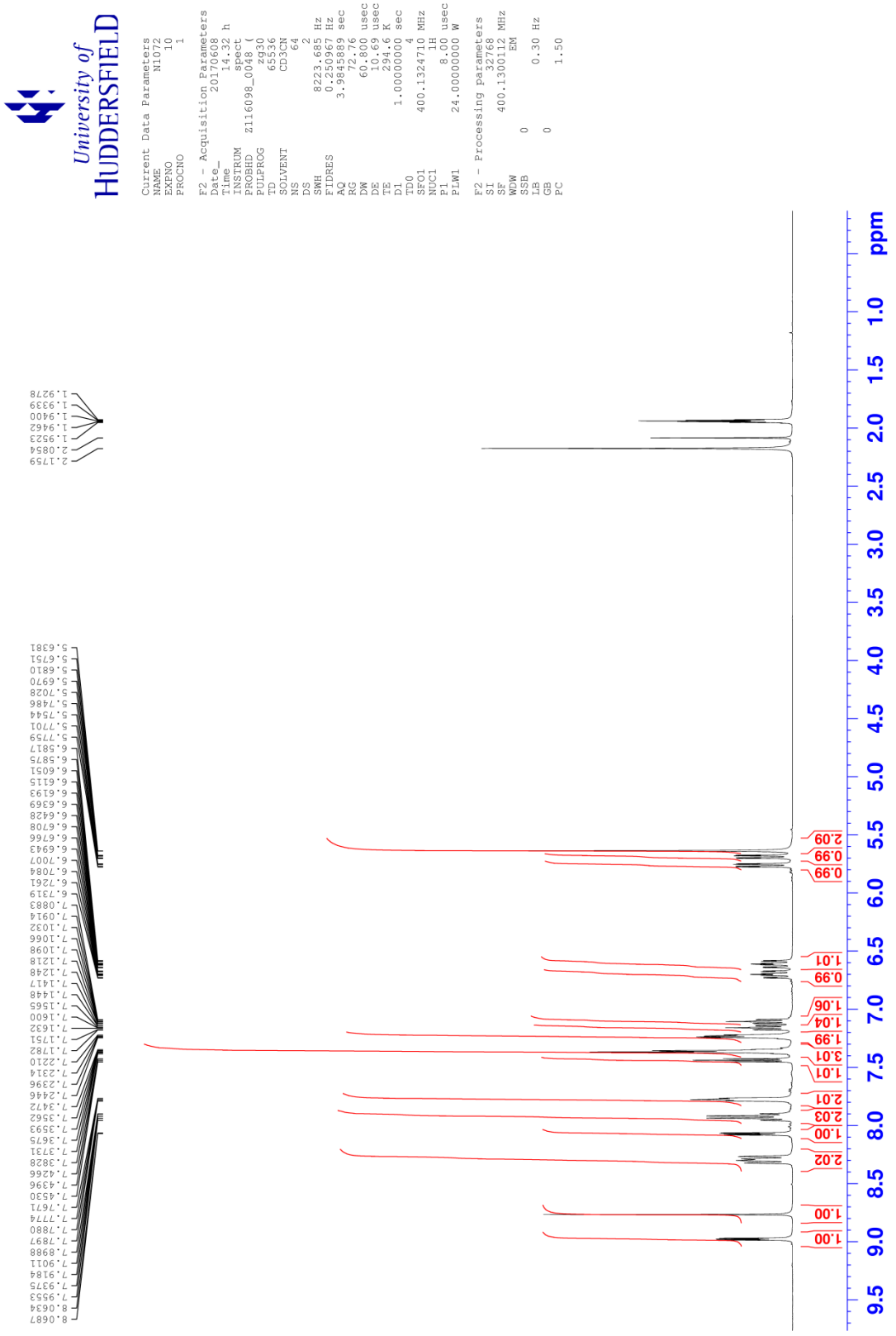

Figure S11 ^{1}H NMR (400 MHz, d_3-MeCN) spectrum of $[(dfppy)_2Ir(pymtz)][PF_6]$ (**2b**)

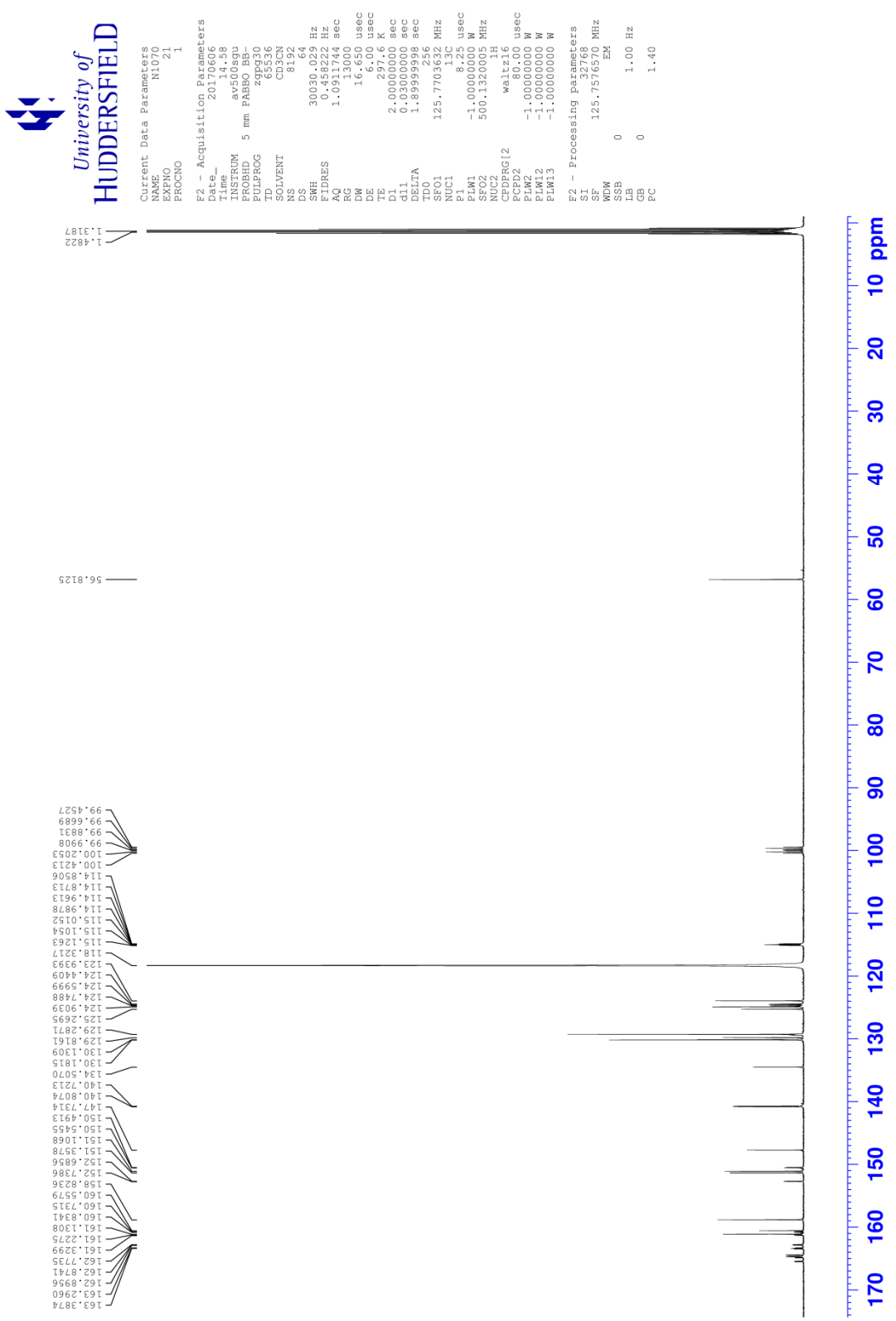

Figure S12 ^{13}C NMR (126 MHz, d_3-MeCN) spectrum of [(dfppy)$_2$Ir(pymtz)][PF$_6$] (**2b**)

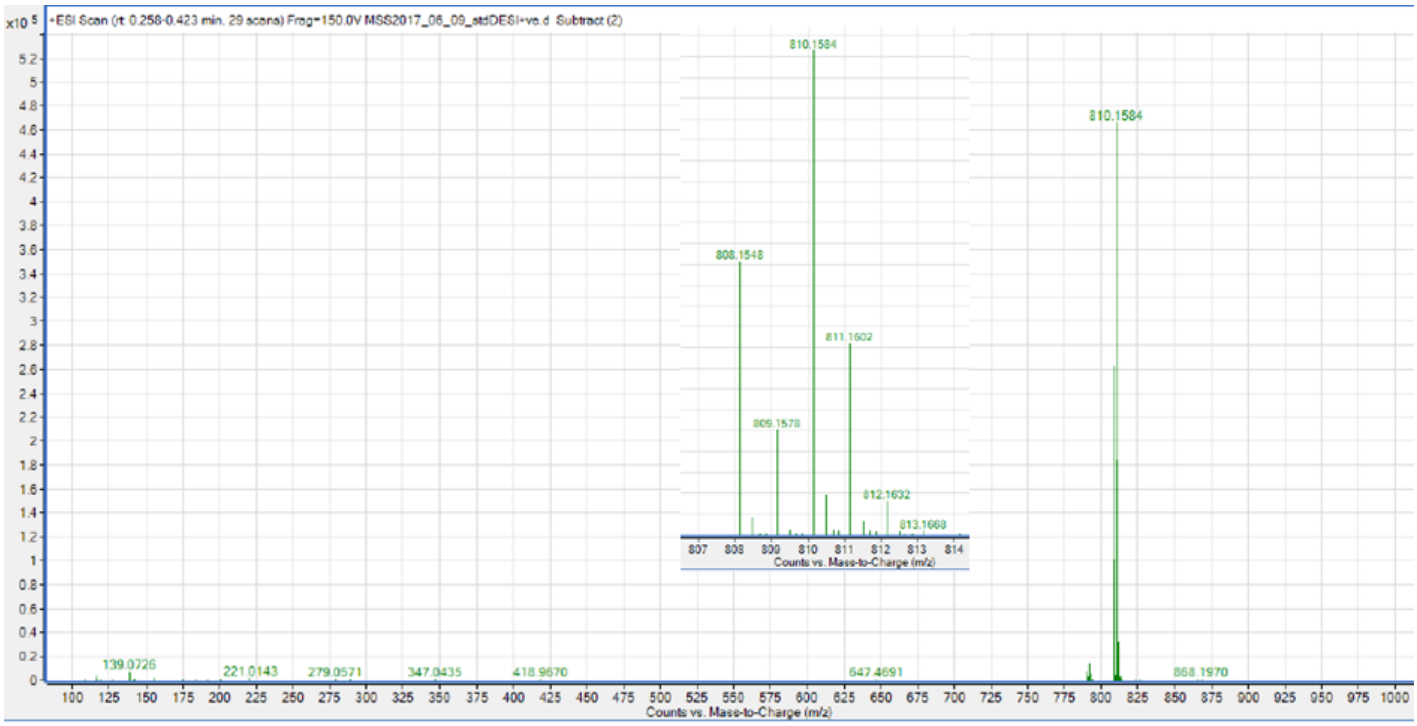

Figure S13 High resolution ESI mass spectrum of $[(dfppy)_2Ir(pymtz)][PF_6]$ (**2b**). The expansion shows detail of the cationic $[C_{35}H_{23}N_7F_4Ir]^+$ mass fragment.

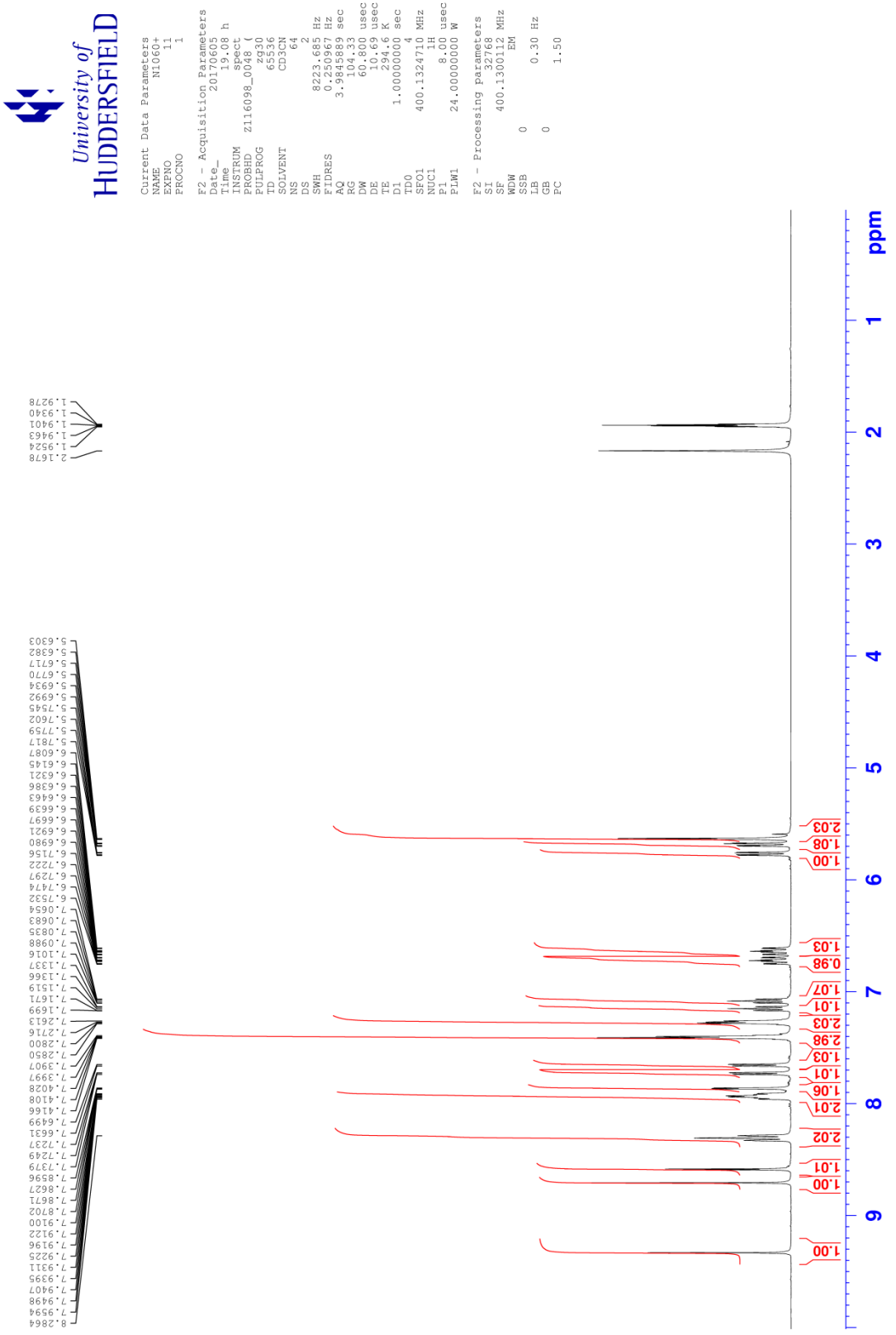

Figure S14 ^{1}H NMR (400 MHz, d_3-MeCN) spectrum of [(dfppy)$_2$Ir(pyztz)][PF$_6$] (**2c**)

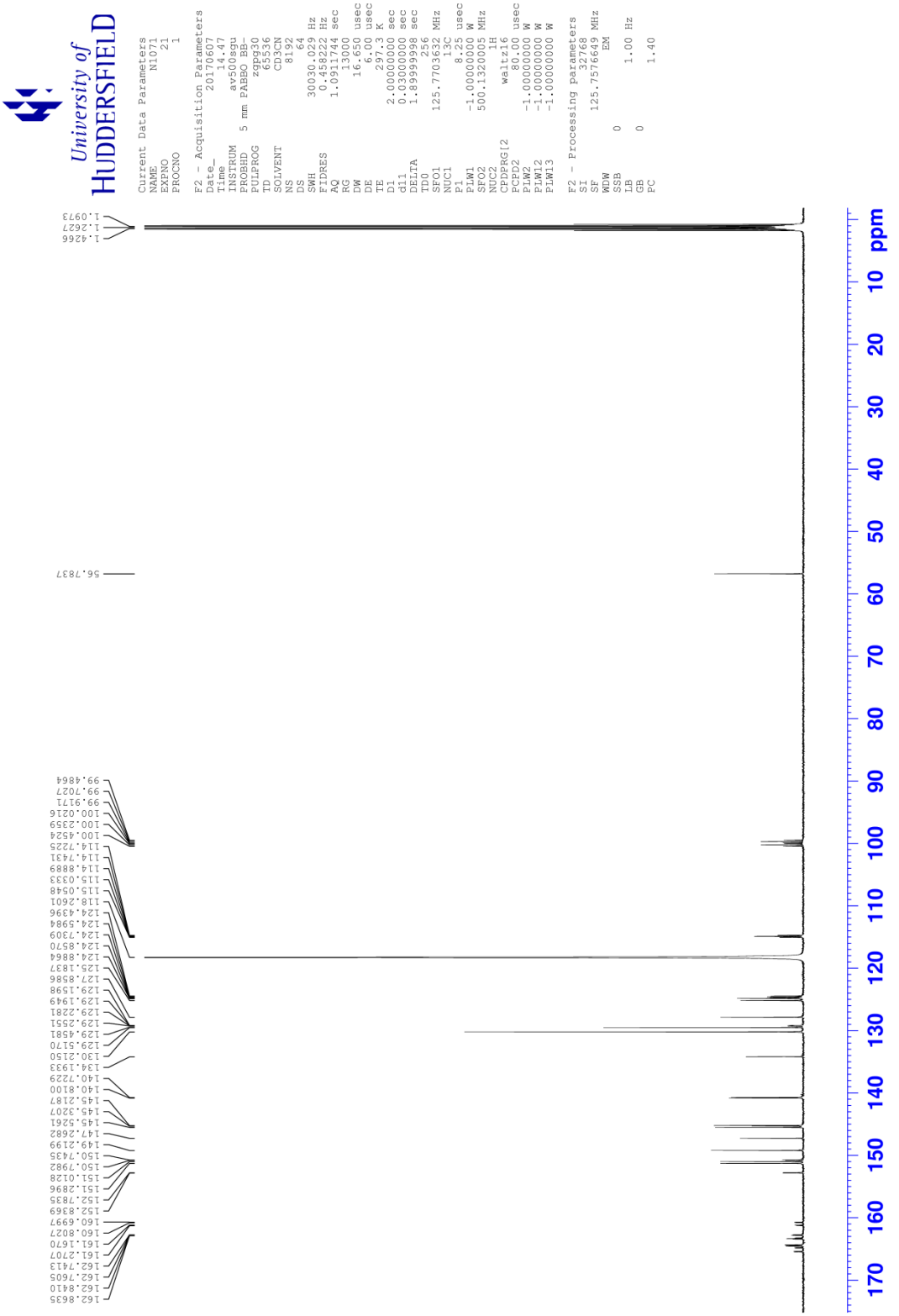

Figure S15 ^{13}C NMR (126 MHz, d_3-MeCN) spectrum of [(dfppy)$_2$Ir(pyztz)][PF$_6$] (**2c**)

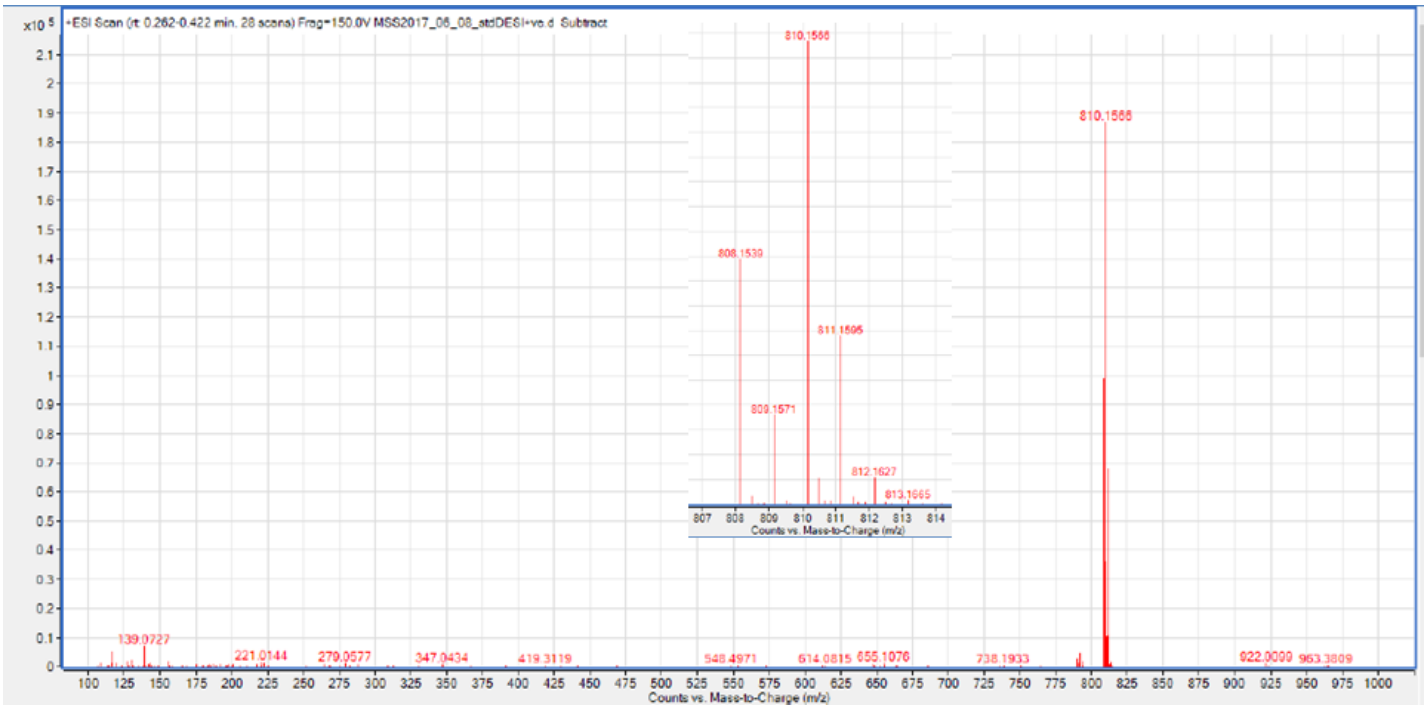

Figure S16 High resolution ESI mass spectrum of $[(dfppy)_2Ir(pyztz)][PF_6]$ (**2c**). The expansion shows detail of the cationic $[C_{35}H_{23}N_7F_4Ir]^+$ mass fragment.

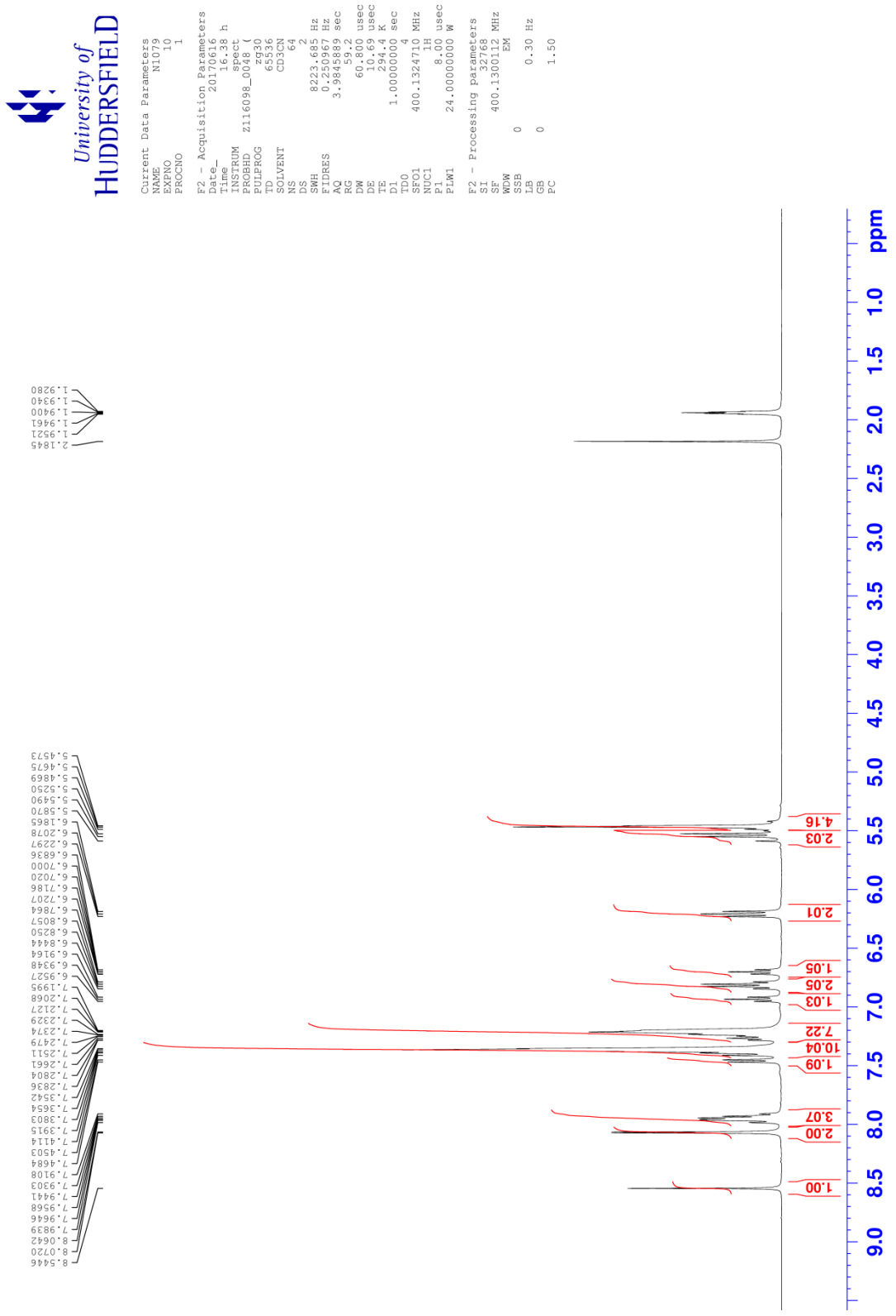

Figure S17 ^{1}H NMR (400 MHz, d_3-MeCN) spectrum of $[(ptz)_2Ir(pytz)][PF_6]$ (**3a**)

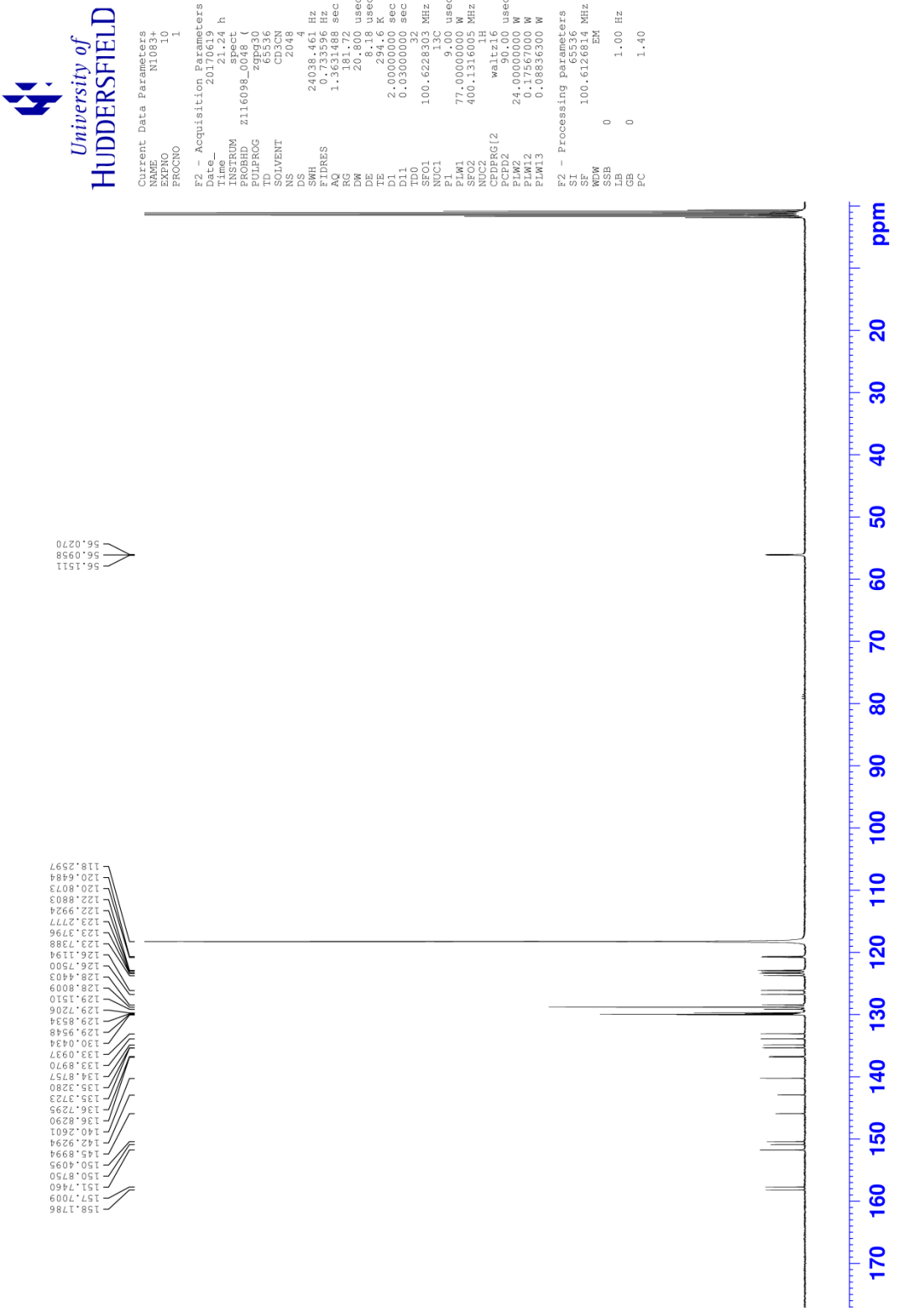

Figure S18 ^{13}C NMR (101 MHz, d_3-MeCN) spectrum of $[(ptz)_2Ir(pytz)][PF_6]$ (**3a**)

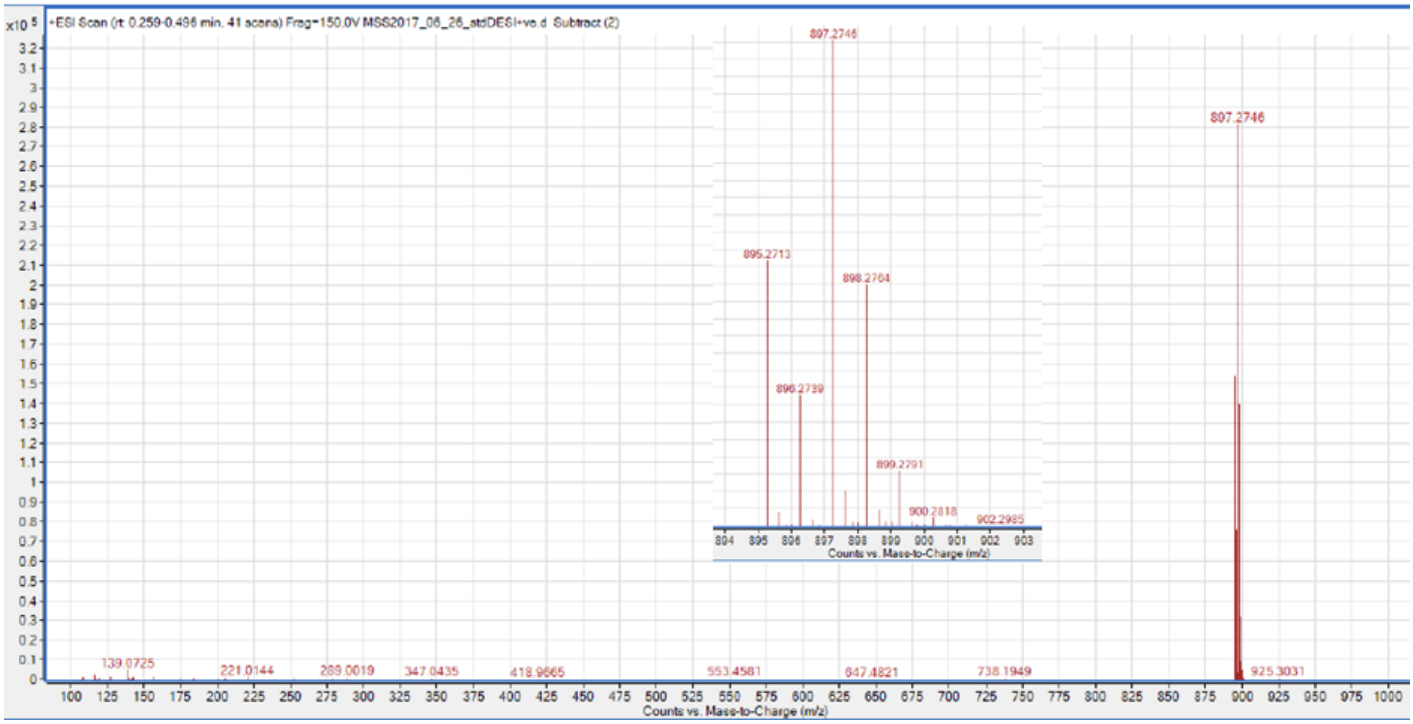

Figure S19 High resolution ESI mass spectrum of $[(ptz)_2Ir(pytz)][PF_6]$ (**3a**). The expansion shows detail of the cationic $[C_{44}H_{36}N_{10}Ir]^+$ mass fragment.

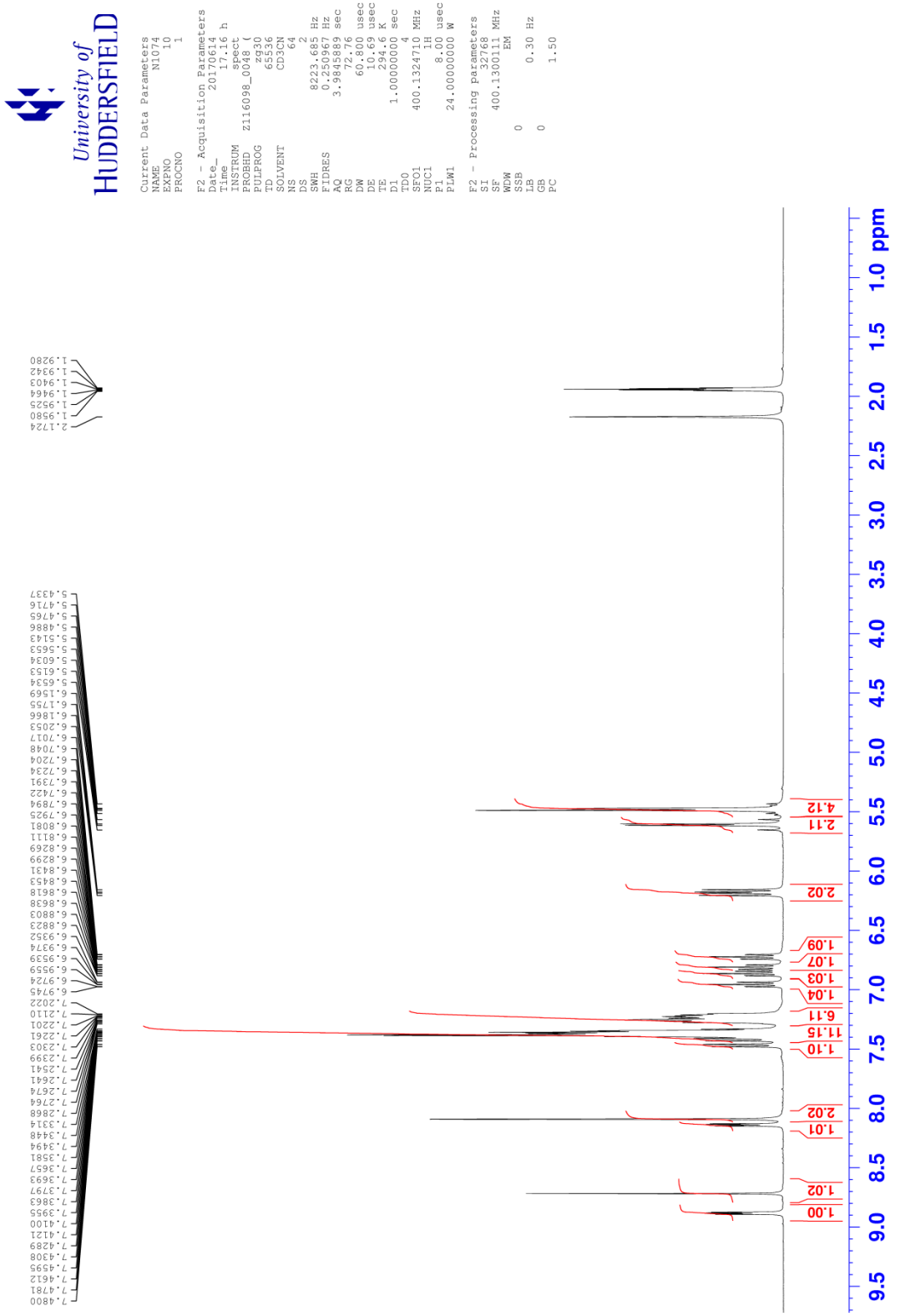

Figure S20 ^{1}H NMR (400 MHz, d_3-MeCN) spectrum of $[(ptz)_2Ir(pymtz)][PF_6]$ (**3b**)

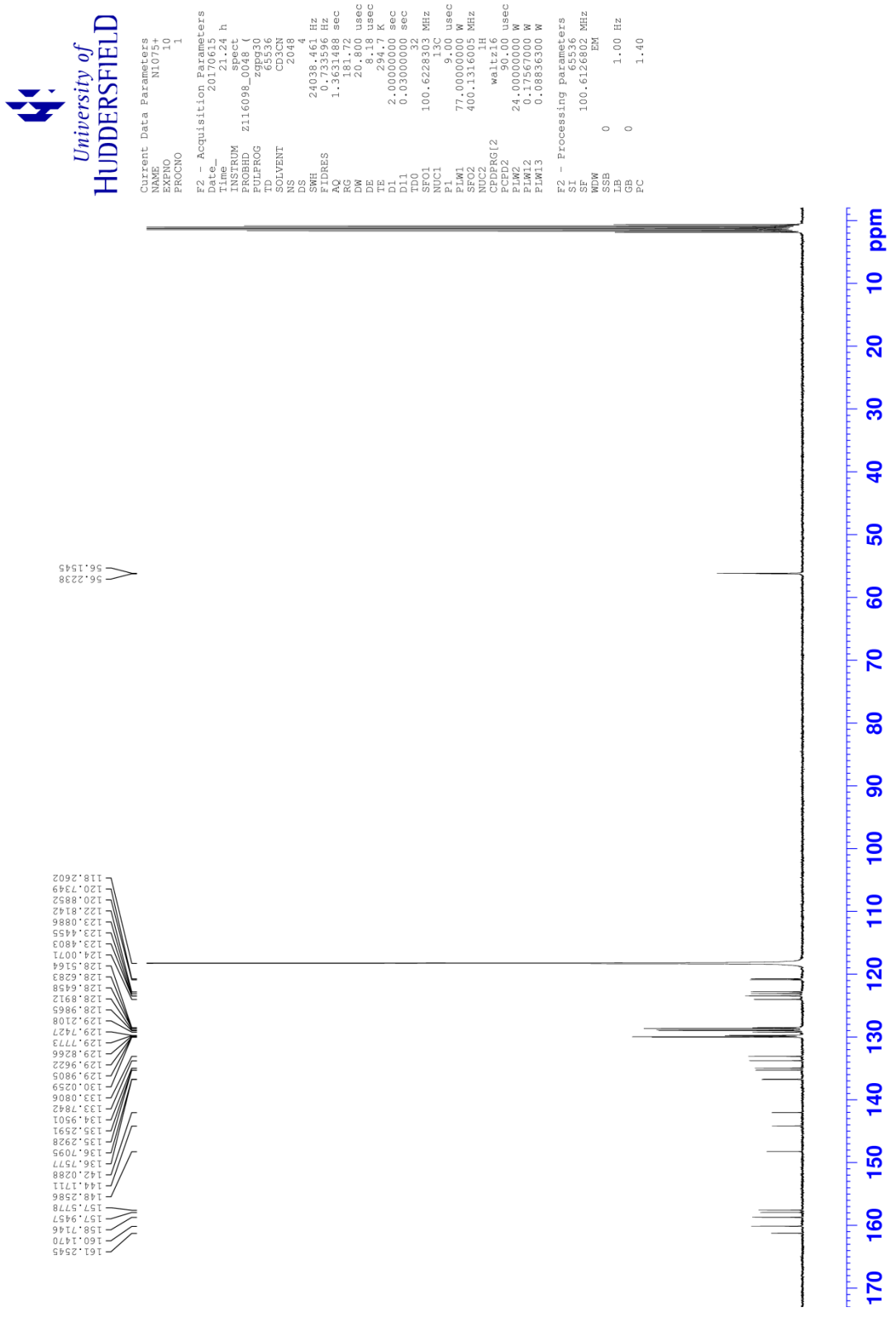

Figure S21 ^{13}C NMR (101 MHz, d_3-MeCN) spectrum of $[(ptz)_2Ir(pymTz)][PF_6]$ (**3b**)

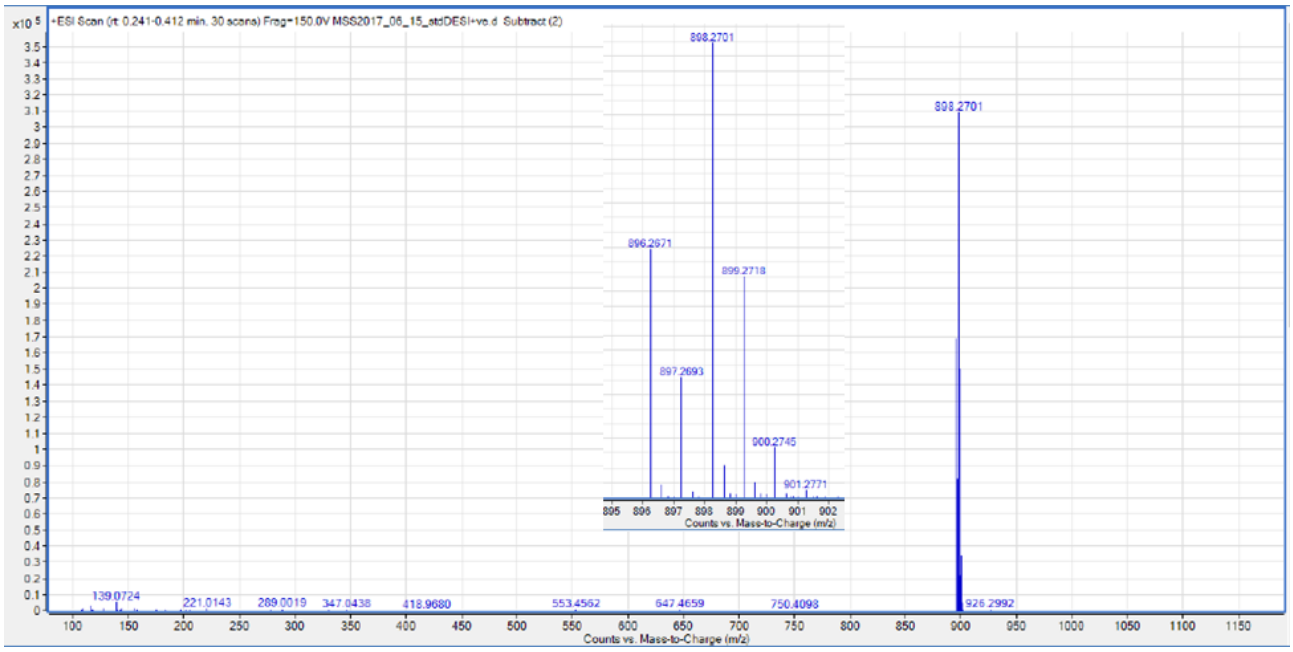

Figure S22 High resolution ESI mass spectrum of $[(ptz)_2Ir(pymTz)][PF_6]$ (**3b**). The expansion shows detail of the cationic $[C_{43}H_{35}N_{11}Ir]^+$ mass fragment.

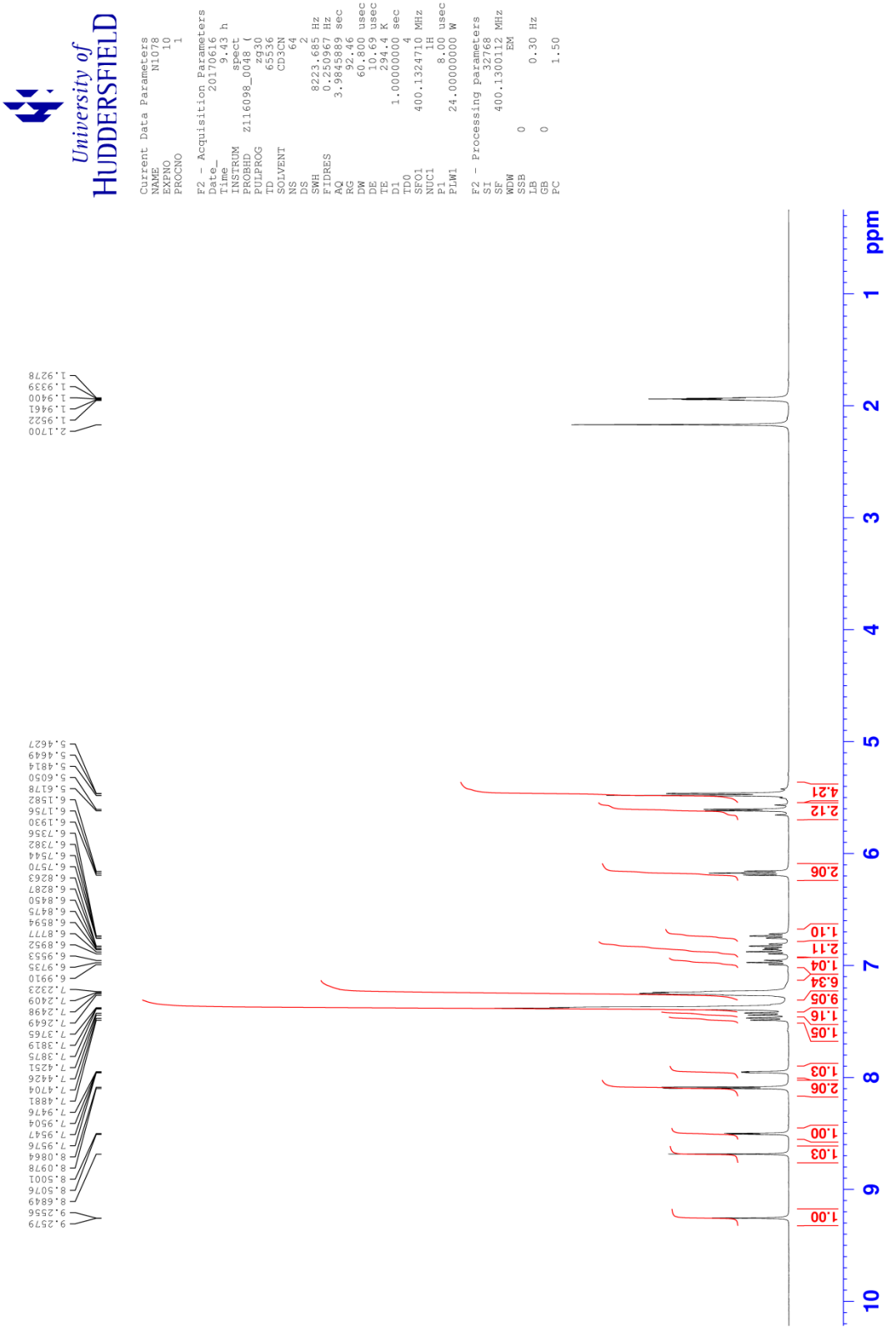

Figure S23 ^{1}H NMR (400 MHz, d_3-MeCN) spectrum of $[(ptz)_2Ir(pyzTz)][PF_6]$ (**3c**)

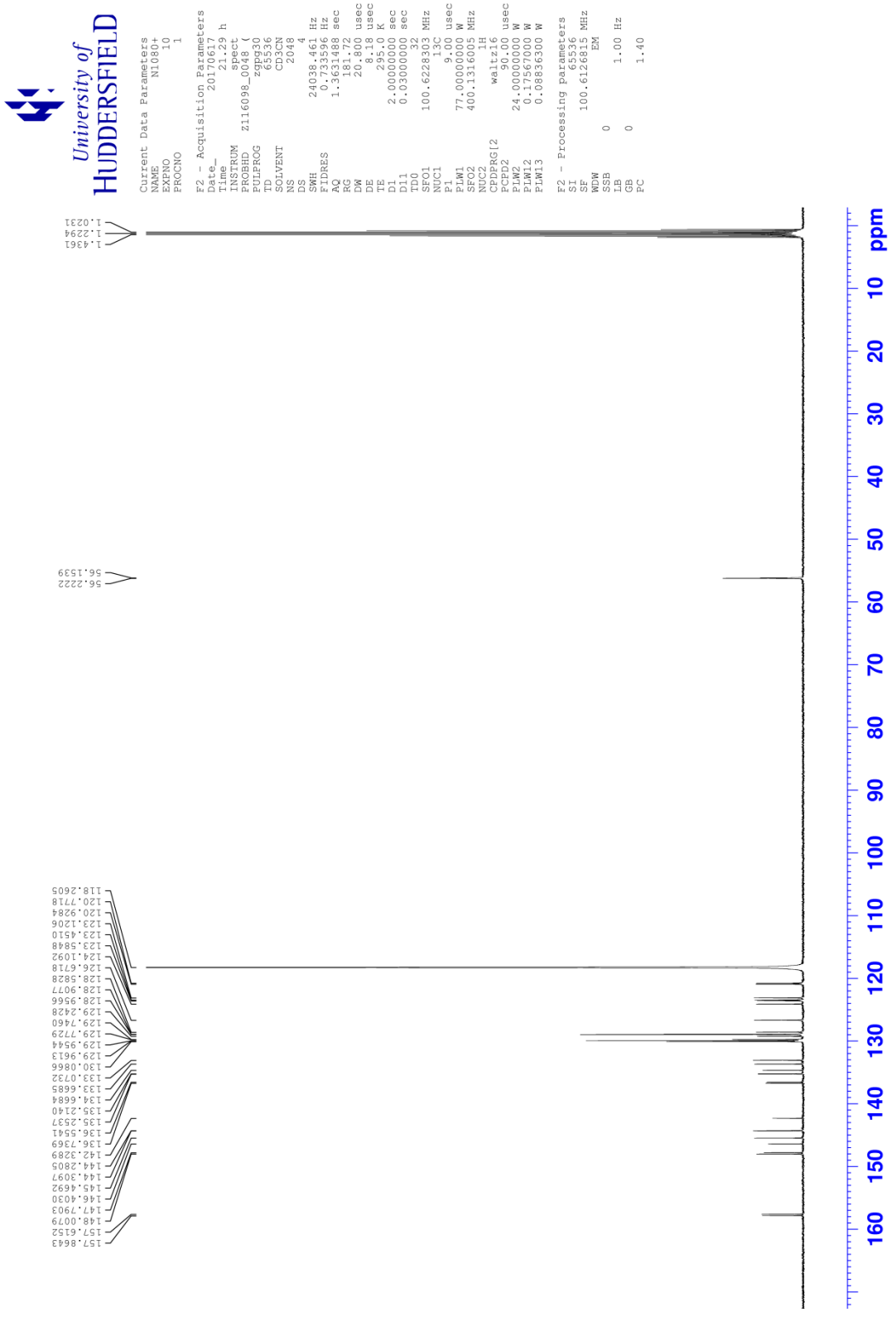

Figure S24 ^{1}H NMR (101 MHz, d_3-MeCN) spectrum of $[(ptz)_2Ir(pyztz)][PF_6]$ (**3c**)

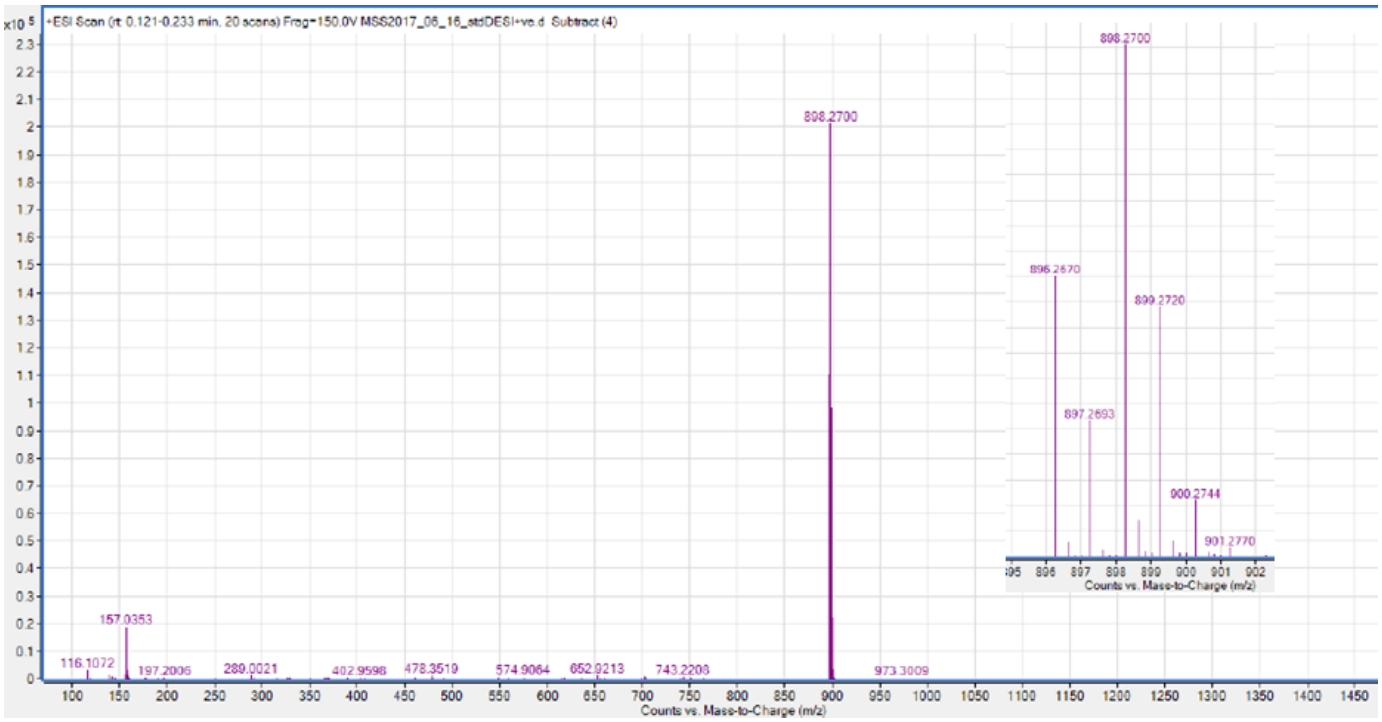

Figure S25 High resolution ESI mass spectrum of $[(ptz)_2Ir(pyztz)][PF_6]$ (**3c**). The expansion shows detail of the cationic $[C_{43}H_{35}N_{11}Ir]^+$ mass fragment.

Crystallography.

Single crystal X-ray diffraction data was collected at 150(2) K on a Bruker D8 Venture diffractometer equipped with a graphite monochromated Mo(Kα) radiation source and a cold stream of N_2 gas. Solutions were generated by conventional heavy atom Patterson or direct methods and refined by full-matrix least squares on all F^2 data, using SHELXS-97 and SHELXL software respectively.[7] Absorption corrections were applied based on multiple and symmetry-equivalent measurements using SADABS.[8]

Crystal for [Ir(dfppy)$_2$(pymtz)][PF$_6$] (**2b**): Crystal data for $C_{35}H_{23}F_{10}IrN_7P$, M = 954.79, *triclinic*, a = 8.6072 (7), b = 13.0303 (11), c = 16.3739 (13) Å, α = 110.320 (2), β = 98.076 (3), γ = 91.353 (3)˚, V = 1699.9 (2) Å^3, T = 150 K, space group *P-1*, Z = 2, 54259 reflections measured, 10477 independent reflections (R_{int} = 0.0502). The final R_1 values were 0.0338 ($I > 2\sigma(I)$). The final $wR(F^2)$ values were 0.0742 ($I > 2\sigma(I)$). The final R_1 values were 0.0450 (all data). The final $wR(F^2)$ = 0.0787 (all data). The goodness of fit on F^2 was 1.0445. CCDC 1953486. The structure contained a positionally disordered phenyl unit which was modelled in two positions using the *PART* instruction. For the six disordered atoms *SIMU*, *DELU* and *ISOR* constrains were used in the least-squares refinement.

Crystal for [Ir(dfppy)$_2$(pyztz)][PF$_6$] (**2c**): Crystal data for $C_{76}H_{46}F_{20}Ir_2N_{14}OP_2$, M = 1997.65, *monoclinic*, a = 15.093 (5), b = 10.413 (3), c = 24.489 (8) Å, β = 94.767 (16), V = 3835 (2) Å^3, T = 150 K, space group *P21/c*, Z = 4, 46042 reflections measured, 11692 independent reflections (R_{int} = 0.0572). The final R_1 values were 0.0469 ($I > 2\sigma(I)$). The final $wR(F^2)$ values were 0.0935 ($I > 2\sigma(I)$). The final R_1 values were 0.0831 (all data). The final $wR(F^2)$ = 0.1055 (all data). The goodness of fit on F^2 was 1.0441. CCDC 1953487. The structure contained a disordered molecule of diisopropylether which was refined using half occupancy (e.g. 10.5) and left isotropic in the least-squares refinement.

Crystal for 1-benzyl-4-(pyrimidin-2-yl)-1,2,3-triazole: Crystal data for $C_{13}H_{11}N_5$, M = 237.27, *monoclinic*, a = 9.5135 (7), b = 10.5680 (10), c = 11.7424 (9) Å, β = 100.156 (3), V = 1162.0 (17) Å^3, T = 150 K, space group *P21/c*, Z = 4, 12387 reflections measured, 2876 independent reflections (R_{int} = 0.0741). The final R_1 values were 0.0556 ($I > 2\sigma(I)$). The final $wR(F^2)$ values were 0.1213 ($I > 2\sigma(I)$). Peak 0.248 eA^3, hole -0.304

eA^3. The final R_1 values were 0.0928 (all data). The final $wR(F^2)$ = 0.1385 (all data). The goodness of fit on F^2 was 1.041. CCDC 1953488.

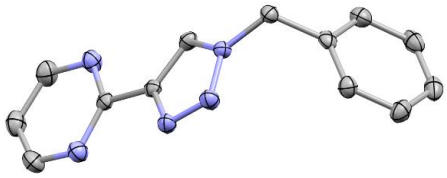

Figure S26. Molecular structure of 1-benzyl-4-(pyrimidin-2-yl)-1,2,3-triazole (pymtz) (hydrogen atoms removed for clarity, ellipsoids at 50 % probability).

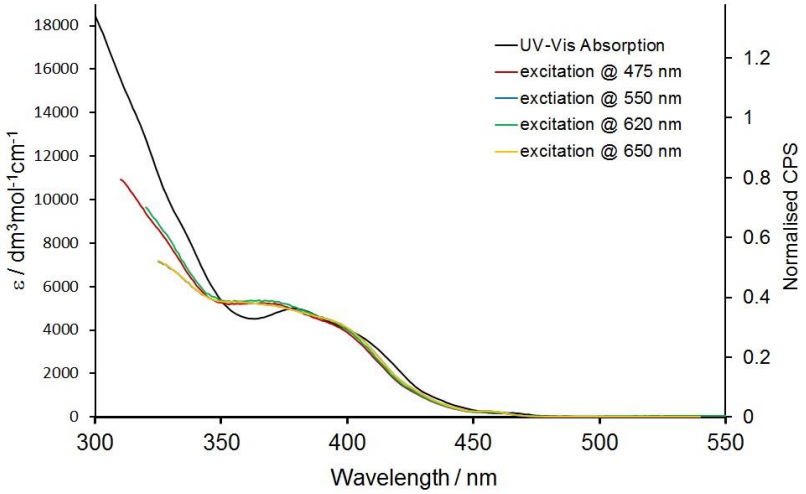

Figure S27. Excitation spectra recorded for aerated room temperature MeCN solutions of **1b**, monitoring photoluminescence at 475, 550, 620 and 650 nm. The UV-Visible electronic absorption profile of **1b** in MeCN is shown for comparison.

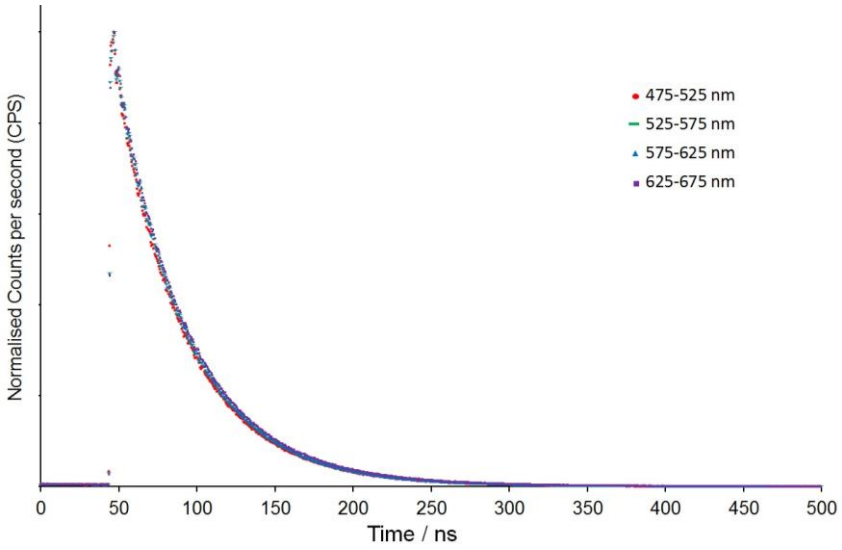

Figure S28. Single photon counting kinetic decay traces obtained for the photoluminescence of **1b** in aerated MeCN solutions. Decay traces were collected over four consecutive 50 nm wide optically filtered windows. Seperate fitting of each data set yielded a photoluminescence lifetime for **1b** of 45 ± 1 ns.

Remark – Solvent-Dependant Dual Emission of 1b

Solvent-dependent emission spectra recorded for **1b** are shown in the main manuscript within Figure 6. Dual emission is observed in all solvents with varying contributions from each of the two emissive states. ^{3}LC emission appears at a λ_{max} that is not influenced by the polarity, unlike λ_{max} of ^{3}LL'CT emission for which a positive solvatochromism was observed with increasing polarity of the solvent. This may be described according to the following equation $\tilde{\nu}_s = \tilde{\nu}_v - \frac{2(\vec{\mu}_T - \vec{\mu}_{GS})^2}{hca_0^3}\left(\frac{\varepsilon-1}{2\varepsilon+1}\right)$, (where $\tilde{\nu}_s$ *and* $\tilde{\nu}_v$ are wavenumbers of the emission maxima in solvent and in vacuum respectively, $\vec{\mu}_T$ *and* $\vec{\mu}_{GS}$ are the permanent dipole moment of the triplet and ground state respectively, ε the dielectric constant of the solvent and the factor hca_0^3 can be considered as a constant in the series of complexes). Indeed we can split the solvents used in our studies into two sets: 2-Me-THF and DCM can be considered as non-polar solvents (s, np) while acetone, acetonitrile and ethanol/methanol mix can be considered as polar solvents (s,p). Calculation of the wavenumber shift ($\tilde{\nu}_{s,p} - \tilde{\nu}_{s,np}$) leads to a negative value for ^{3}LL'CT. Consequently, λ_{max} in the polar solvent will be red-shifted with respect to λ_{max} in the non-polar solvent. This is the trend observed in figure 6. Concerning ^{3}LC emission, the difference between the magnitude of the excited-state and ground-state dipole moment ($\mu_T - \mu_{GS}$) is zero, thus the effect of the solvent polarity is removed and the ^{3}LC emission is solvent insensitive. This semi-quantitative reasoning does not exclude more subtle interactions which may affect emission maxima, such as potential Coloumbic interactions between complex and counter-ion.

Table S1 Summarised lifetime data obtained from variable temperature photoluminescence spectroscopy of 2Me-THF solutions of **1a-2c** at 100 K and 295 K. ([a] 315 K).

	τ / ns	
	100 K	**295 K**
1a	4471	95
1b	4680	37[a]
1c	4491	117
2a	5262	404
2b	5944	89
2c	5073	365

Transient Absorption

A broadband ultrafast pump-probe transient absorbance spectrometer 'Helios' (Ultrafast Systems LLC) was used to collect data over a 3 ns time window with a time resolution of around 250 fs. A Ti:sapphire amplifier system (Newport Spectra Physics, Solstice Ace) producing 800 nm pulses at 1 kHz with 100 fs pulse duration was used to generate the probe beam, and to pump a TOPAS Prime optical parameter amplifier with associated NirUVis unit to generate the excitation beam. The probe beam consisted of a white light continuum generated in a CaF_2 crystal and absorbance changes were monitored between 340 and 620 nm. Samples were excited with 0.5 μJ at 285 nm and were contained in 0.2 mm path length quartz cuvettes and magnetically stirred during measurements. Before data analysis the pre-excitation data were subtracted and spectral chirp was corrected for.

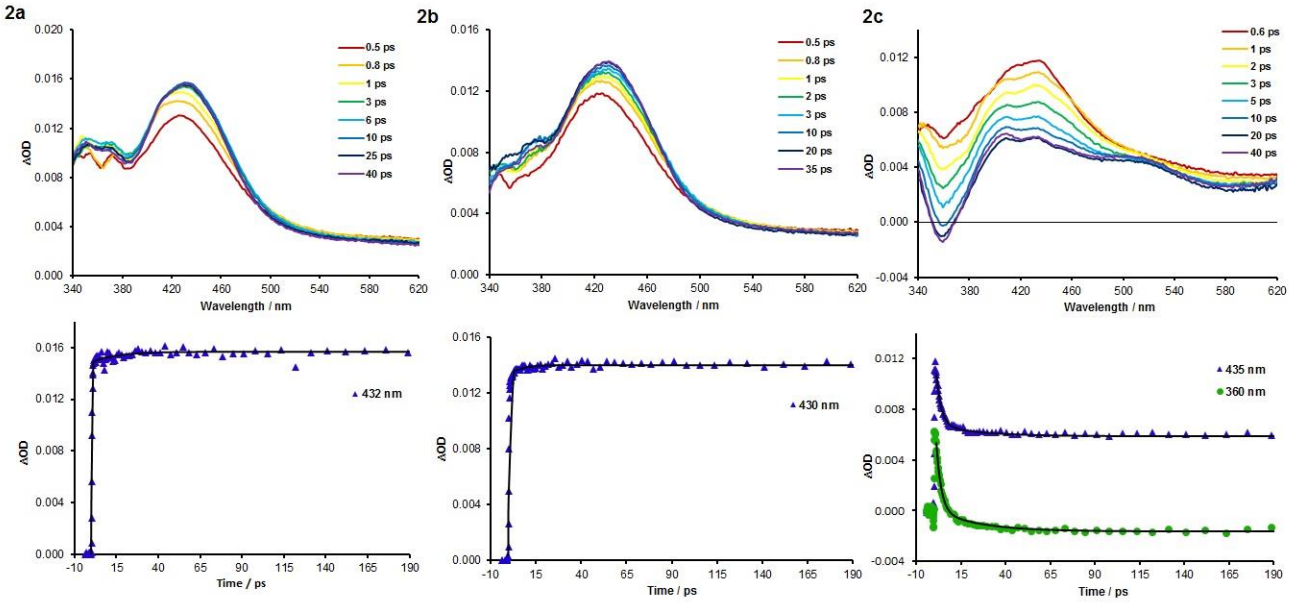

Figure S29 Top: Chirp-corrected transient absorption spectra at selected time delays for MeCN solutions of complexes **2a**-**2c** (λ_{ex} = 285 nm). Bottom: Associated decay traces at representative wavelengths for **2a**-**2c**. Markers show experimental data. Solid lines correspond to fitting curves generated through global analysis.

Table S2 Summarised kinetic time constants obtained through global analysis for transient absorption spectra of complexes **1a**-**2c** and **2a**-**2c** in MeCN solutions with excitation at 285 nm.

	Rise		Decay	
	τ_1 / ps	τ_2 / ps	τ_1 / ps	τ_2 / ps
1a	0.20 ± 0.01	15.41 ± 0.52	-	-
1b	0.15 ± 0.01	-	12.62 ± 0.12	-
1c	0.09 ± 0.01	-	0.96 ± 0.01	21.82 ± 0.35
2a	0.23 ± 0.01	14.91 ± 1.00	-	-
2b	0.25 ± 0.01	5.68 ± 0.24	-	-
2c	0.18 ± 0.01	-	2.72 ± 0.03	24.62 ± 0.79

Computational details

All calculations have been performed with ORCA Quantum Chemistry software.[9] [10] The structures of all complexes, in their respective ground and lowest excited triplet states, have been fully optimized at the DFT/(U)DFT levels with hybrid functional B3LYP,[11, 12] including Grimme's dispersion correction (D3-BJ),[13, 14] with a triple-ζ Ahlrichs basis set, namely def2-TZVP(-f), with a p polarization function for the H atoms, two d polarization functions for the second row elements, and for the iridium the triple-ζ basis set def2-TZVPP with two f and one g polarization functions and its associated relativistic effective core potential.[15] Following geometry optimizations, vibrational frequency analyses were performed at the same level of theory to verify the nature of the stationary points. The absorption spectra have been calculated by means of TD-DFT/B3LYP applied to the lowest 40 states. In these TD-DFT calculations the resolution-of-identity (RI) approximation for hybrid functionals (as implemented in ORCA) was employed to calculate the Coulomb energy term using the Ahlrichs/Weigand Def2-TZV basis as the auxiliary basis set and the exchange term by the so-called 'chain-of-spheres exchange' (COSX) algorithm. In order to analyse the nature of the electronic transitions in the TD-DFT spectra, the Natural Transition Orbitals (NTO) were computed. Previous studies have shown that B3LYP accurately reproduces structural and energetics of Ir(III) complexes. [16, 17] Solvent effects were simulated using the Solvation Model (SMD) that has been proposed by Cramer and Truhlar.[18]

Acetonitrile, tetrahydrofuran and ethanol were used as solvent in this work in order to employ the same solvents as those used in the experimental work.

Minimum energy paths were optimized in SMD-MeCN[18] with the nudged elastic band (NEB) method [19, 20] using a python module developed in the Clancy group that is interfaced with Orca.[21] A 10-frame initial path was prepared by interpolating start and end geometries using the IDPP method.[22]

The IMDHO(T) model in ORCA_ASA was used to compute vibrationally resolved electronic spectra.[23] This procedure includes vibrational effects in a pure harmonic approximation for ground and excited states,

without taking into account Duschinsky effects. To generate the vibrational emission spectra corrected by vibrational effects, ORCA_ASA uses the optimized ground and excited state minima and the corresponding Hessians. IMDHO(T) model is based on two approximations which can influence the quality of the results. The first approximation consists in assuming that the vibrations of the excited state are the same as those of the ground state, the second one might be more severe as it considers that emission occurs at a point of the potential energy surface that is still on the harmonic part of the PES of the relaxed excited state neglecting the effect of relaxation on the transition moments. This procedure requires the calculation of the displacement of the excited state equilibrium geometry relative to the ground state geometry in dimensionless normal coordinates (DDNC). The Huang-Rhys factors frequently used to analyse experimental resolved emission spectra are related to the square of the DDNC values used in our analysis. [24] Here, DDNC calculations also serve to identify the vibrational modes involved in the conversion between different types of triplet states, i.e ^{3}MLCT/^{3}LC vs. ^{3}MLCT/^{3}LL'CT. To simulate the spectral broadening we use a Gaussian convolution with an effective FWHM of 320 cm^{-1} at 0 K.

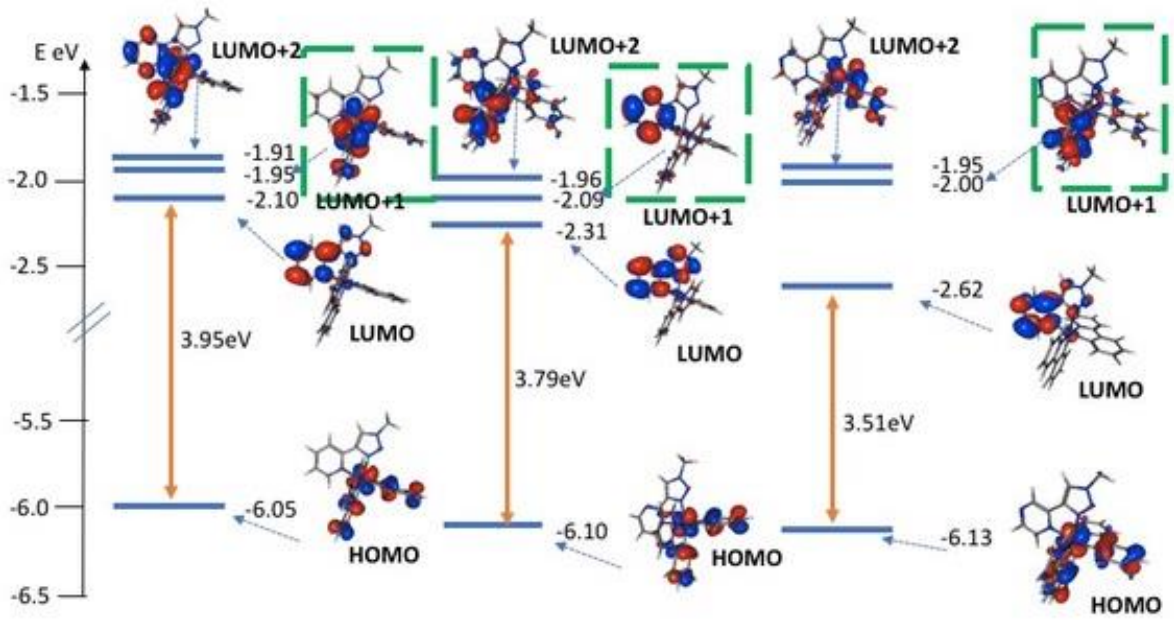

Figure S30. Molecular orbital energies and isosurface plots for HOMO to LUMO+2 for complexes **2a** (left), **2b** (middle) and **2c** (right). The green square highlights LUMO+1, whose localisation varies.

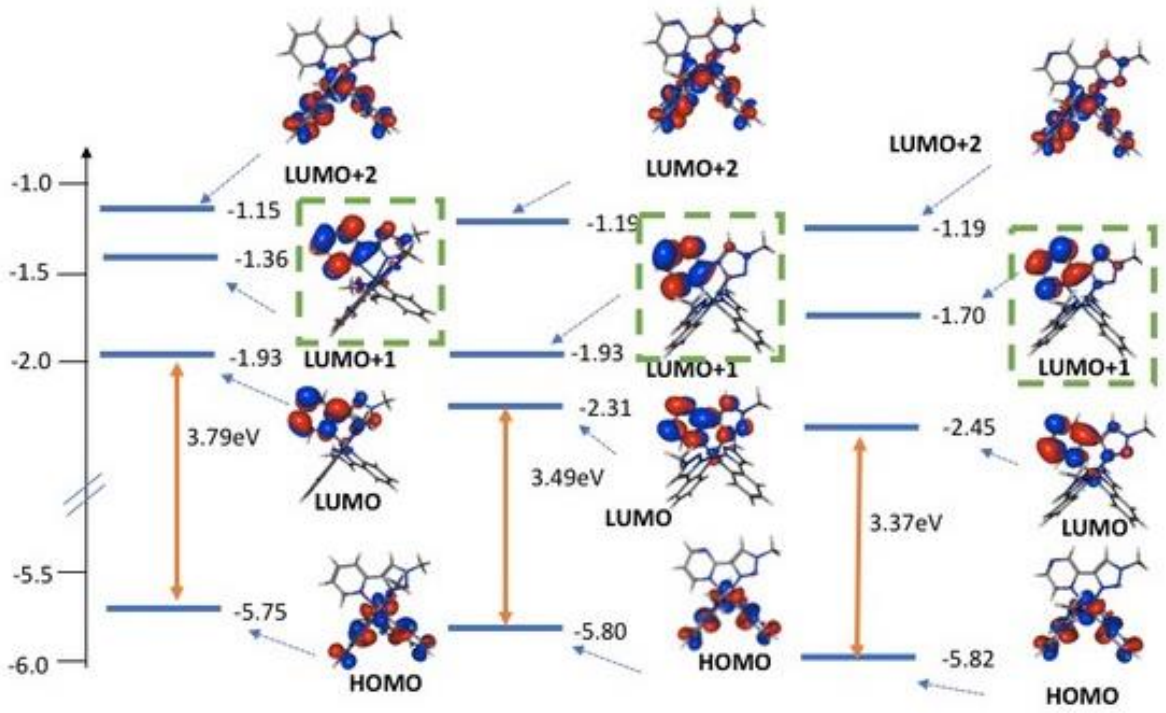

Figure S31. Molecular orbital energies and isosurface plots for HOMO to LUMO+2 for complexes **3a** (left), **3b** (middle) and **3c** (right). The green square highlights LUMO+1 whose localisation differs that those of ppy and dfppy complexes with pytz and pyztz ancillary ligands.

Figure S32. Spin densities for computed ^{3}MLCT/^{3}LC and ^{3}MLCT/^{3}LL'CT states of complexes **1a** to **3c** in MeCN using SMD model.

	^{3}MLCT/^{3}LC	^{3}MLCT/^{3}LL'CT
1a	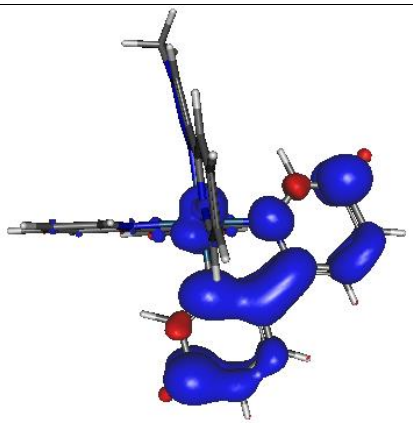 left	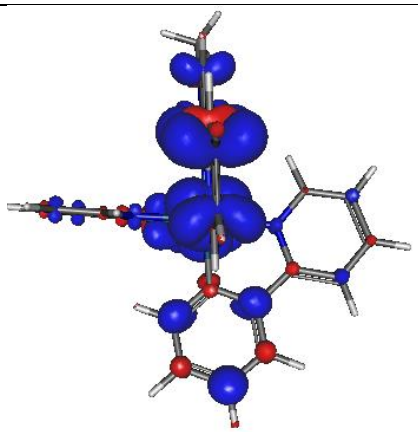

1b	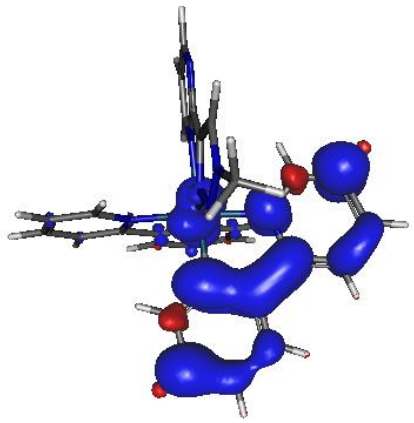 right	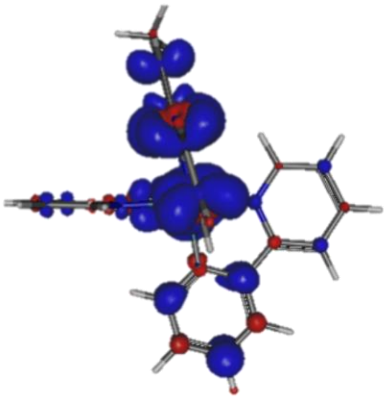
1c	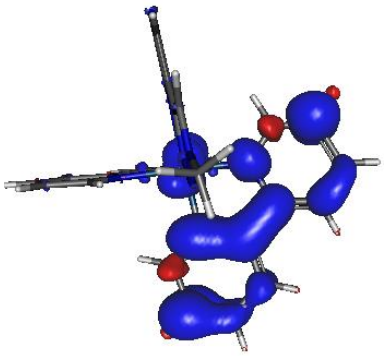 right	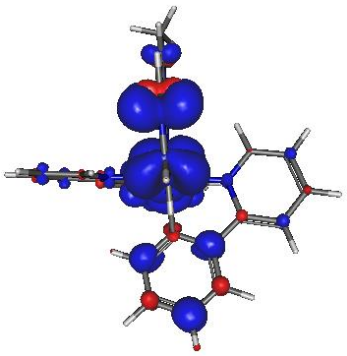
2a	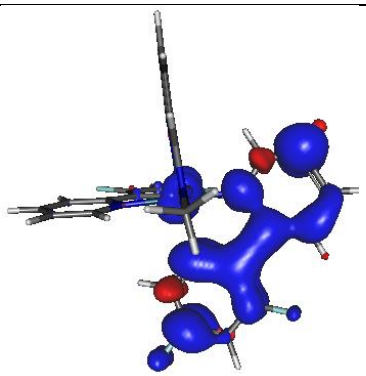 right	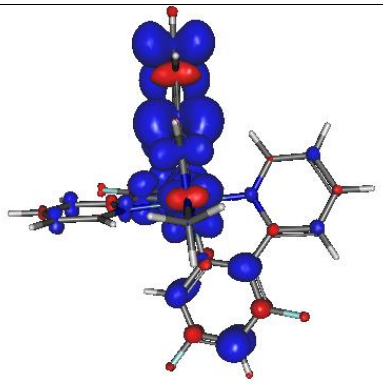

2b	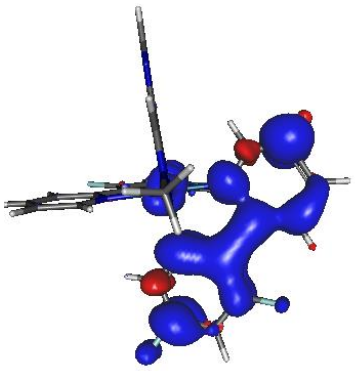 right	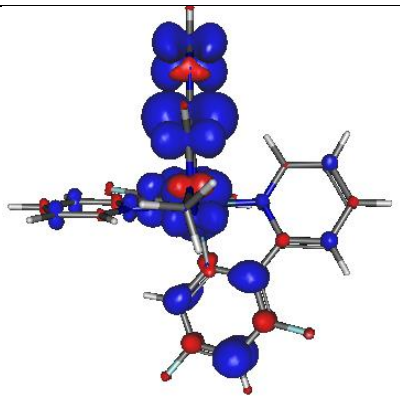
2c	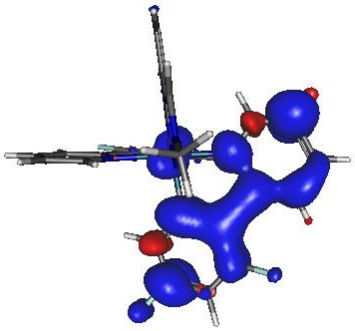 right	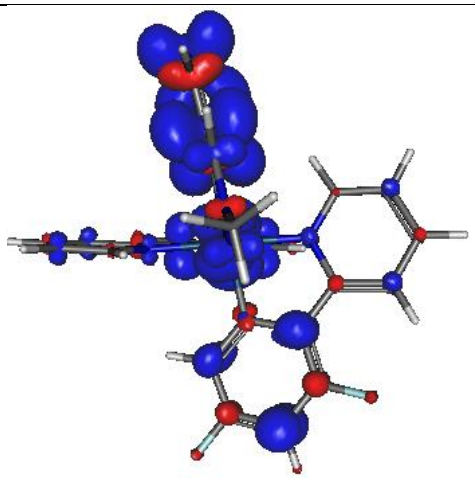
3a		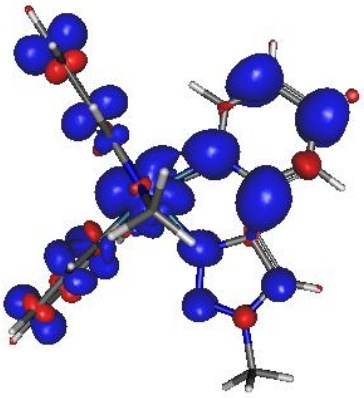
3b		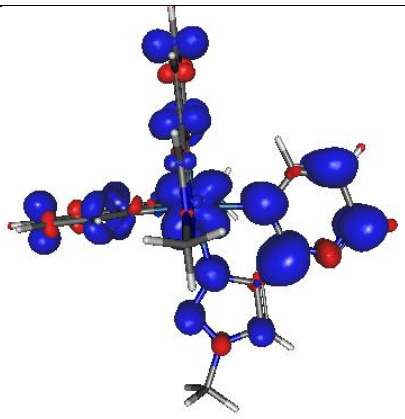

3c		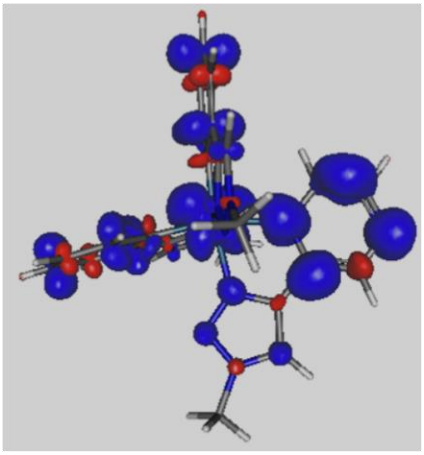

In order to confirm interpretations of the experimental electrochemical data, calculations were carried out to optimise the doublet states deriving from oxidation and reduction of the complexes. The observed localisation for the spin densities of the dicationic oxidised forms of the complexes are well matched to the distributions of the HOMO for the monocationic closed-shell forms of the complexes (Figure S33). In the case of the singly reduced charge neutral forms, the spin density is localised on the N^N ancillary ligand with the unpaired electron exhibiting greater localisation on the 6-membered heterocycle. Plots of the experimentally derived E_{ox} and E_{red} against calculated HOMO and LUMO energies respectively give a good correlation, as do plots of E_{ox} and E_{red} against the calculated adiabatic energy differences between the oxidised form and ground state and the reduced form and ground state respectively (Figure S33).

Figure S33. Spin densities for computed one-electron oxidised and reduced forms of complexes **1a** to **3c** in MeCN using SMD model.

	Oxidised	**Reduced**
1a	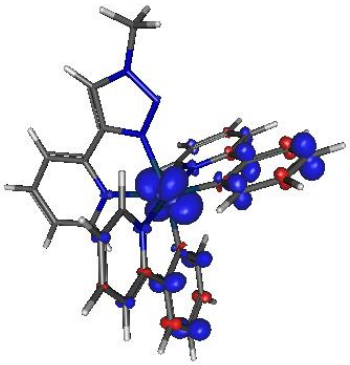	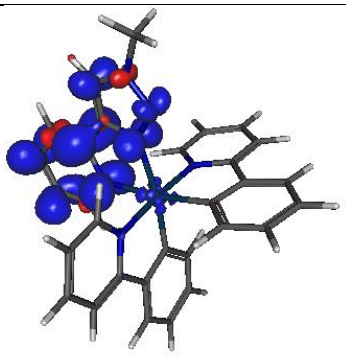

1b	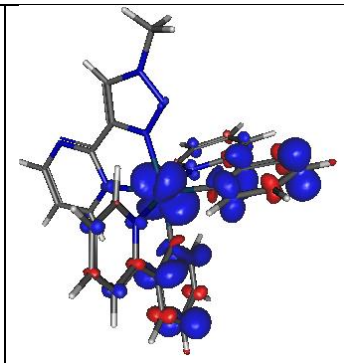	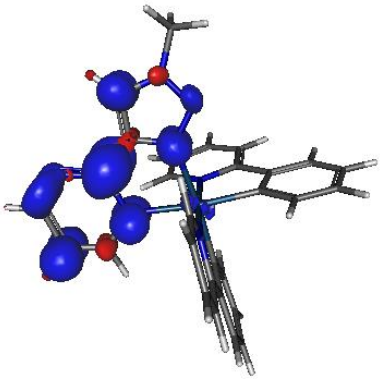
1c	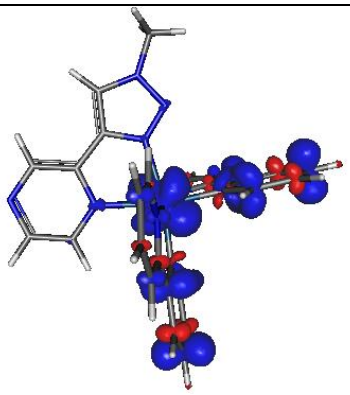	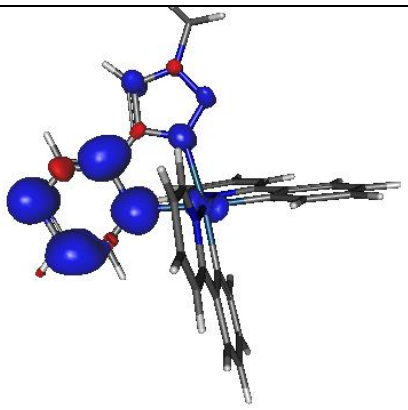
2a	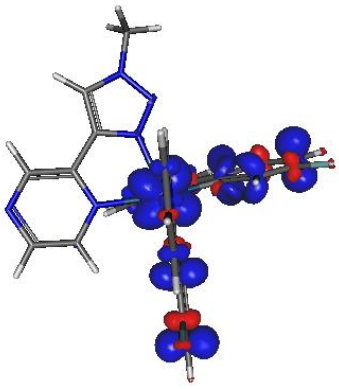	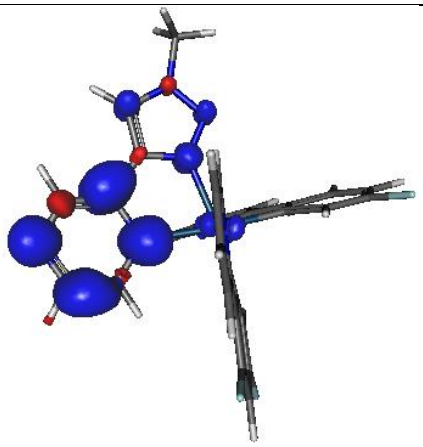
2b	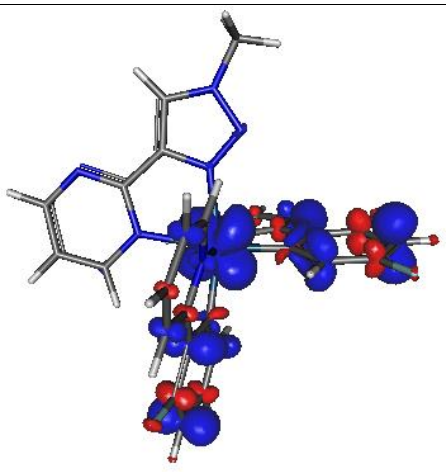	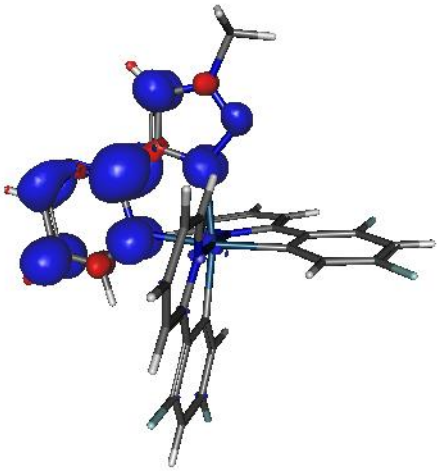

2c	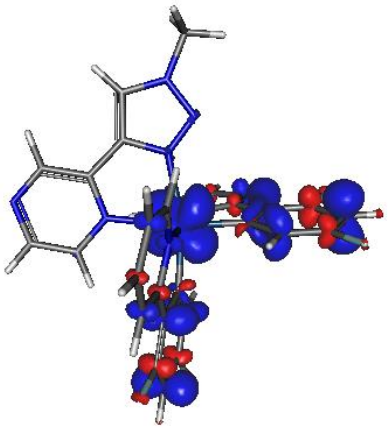	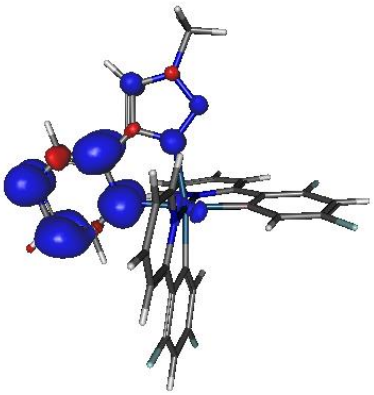
3a	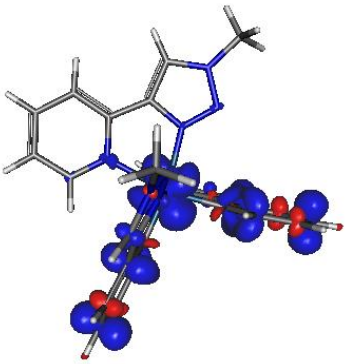	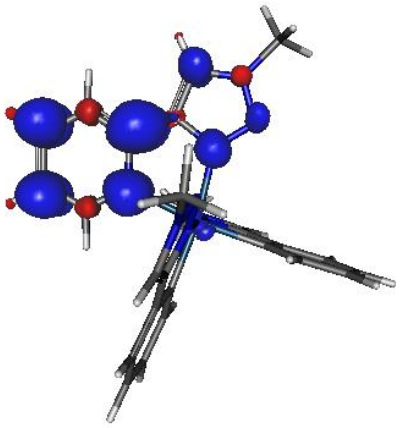
3b	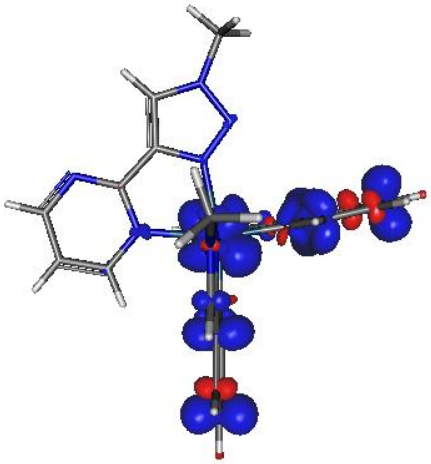	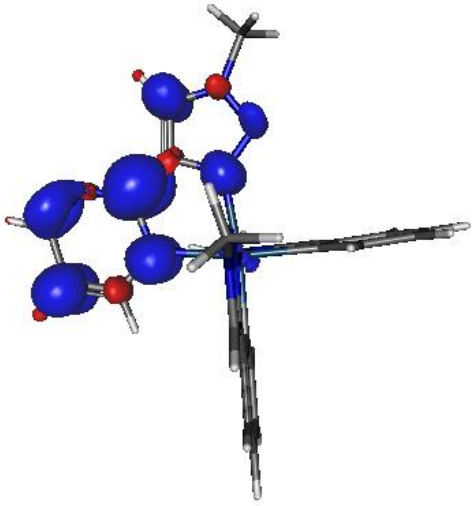

3c	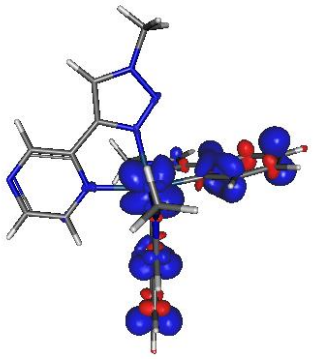	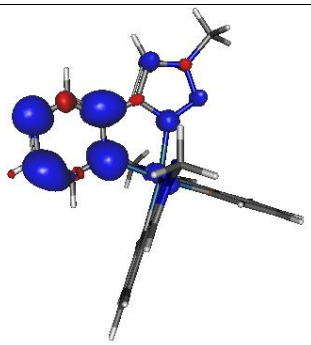

TD-DFT calculated absorption spectra

UV-visible absorption spectra were calculated using time-dependent DFT calculations and are shown in Figure S34. The calculated spectra agree well with those obtained experimentally with the spectra for **3a-c** exhibiting the most blue-shifted absorption profiles. Calculations confirm the assignment of features at 250 to 300 nm as arising from $\pi \rightarrow \pi^*$ ^{1}LC transition associated with the N^N and C^N ligands with transitions at lower energies having ^{1}MLCT character.

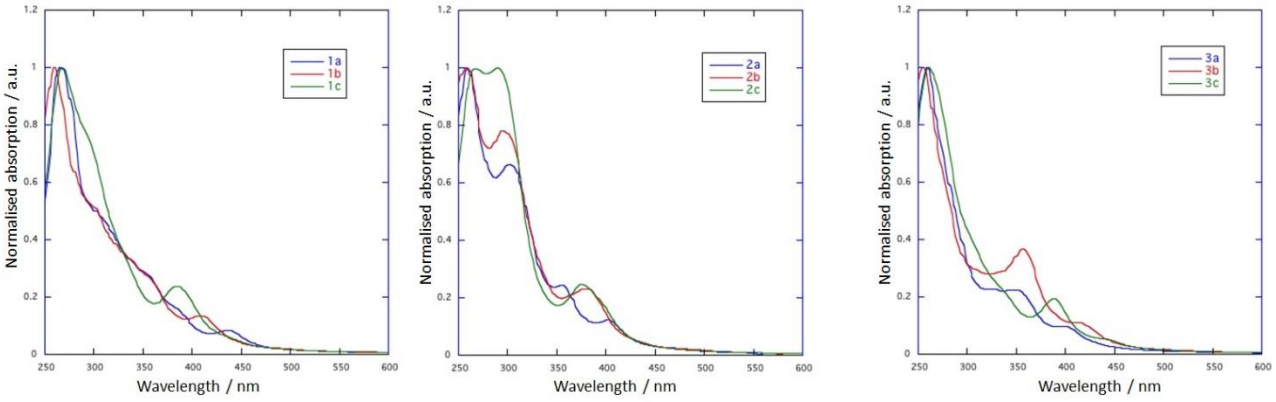

Figure S34. Calculated UV-visible absorption spectra for complexes **1a** to **3c** in MeCN using SMD model.

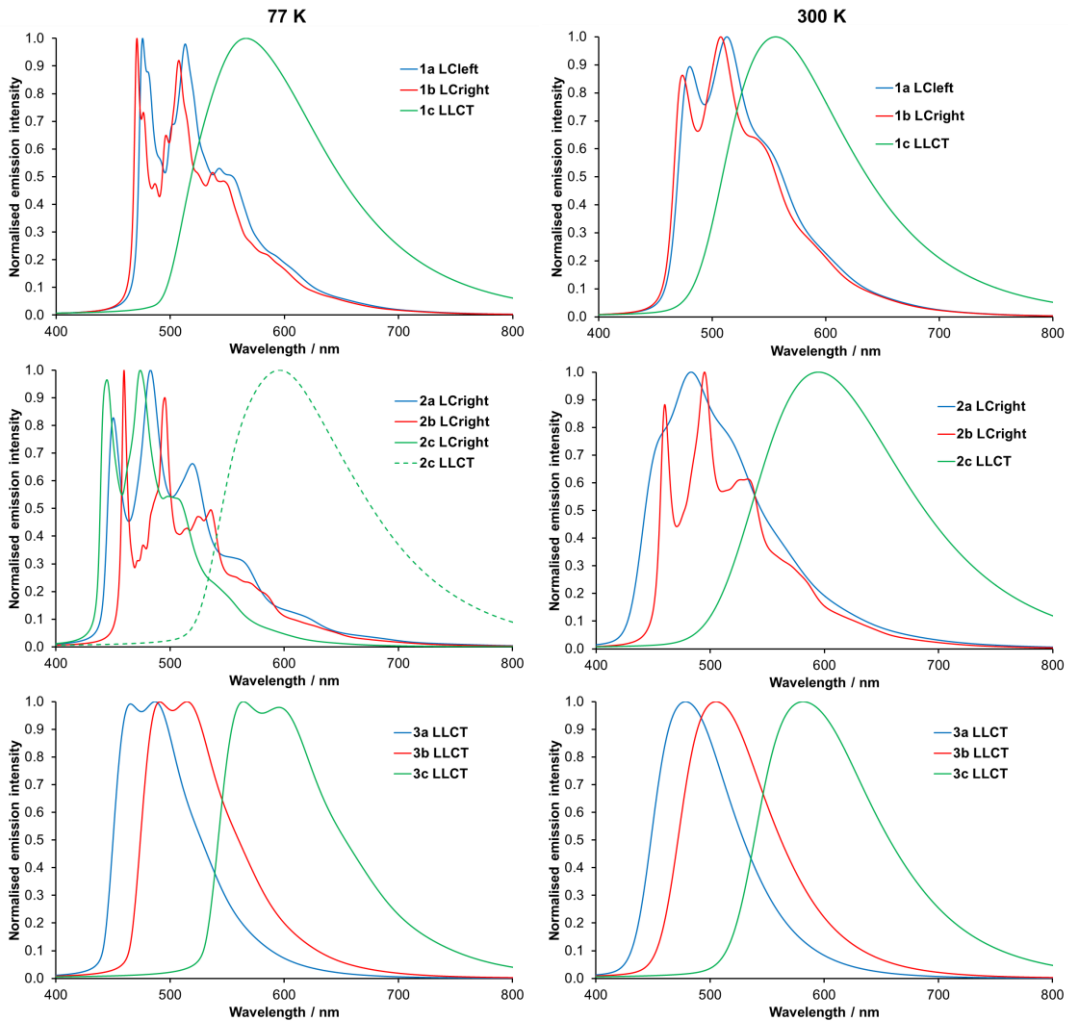

Figure S35. Vibrationally resolved emission spectra for the ^{3}MLCT/^{3}LC and ^{3}MLCT/^{3}LL'CT states of **1a** to **3c** at 77 and 300 K (SMD: ethanol).

Theoretical analysis of the vibronic emission spectra of compound 1a.

Emission spectra from ^{3}MLCT/^{3}LC states present marked structures and to the best of our knowledge, theoretical calculations are very scarce.[25]

The simulated emission spectra from ^{3}MLCT/^{3}LC states studied here are very similar, so we decided to focus on complex **1a** to provide a better understanding of the emission bandshape of this family of complex.

The agreement between experiment and theory is good and the main experimental features are accurately reproduced despite a slight underestimation of the relative intensity of the $E_{0\text{-}0}$ transition. The DDNC, which describe geometry deformation, collected in Figure S37 clearly show that only a very complex combination of modes, i.e multi-mode, can explain the bandshape. Hence to identify the vibrations at the origin of the multi-peak emission spectrum, we have adopted the following protocol :

(i) firstly we simulate the luminescence spectrum by neglecting all the displacements, consequently all the vibronic effects (insert in Figure S36a) disappear,

(ii) secondly we restore the effect of each vibration one by one (Figure S36a-f) by giving to the displacement shift its initial value. Doing so, we have identified six groups of frequencies named $\nu_{eff,1}$ to $\nu_{eff,6}$.

At the end of this procedure, the "step by step" simulated spectrum (Figure S36f) must reproduce the initial one. Our analysis shows that these emission spectra can be viewed as several superimposed progressions of different bandshapes. Contributions are due to mixed excitation of several effective vibrational modes (C-C, C-N, stretching, C-H wagging and valence deformation such as CCH, CCC, CCN of phenylpyridine and ancillary ligand) and are spread over the three bidentate ligands. The major structuration (Figure S36a), i.e the most intense peaks, arises from a combination of modes ($\nu_{eff,1}$ = 157-154 and 149-147) describing collective stretches as C-C and C-N coupled with CH wagging motions (see Figure S36a pink arrows, Figures S37 and S38) and progresses by an interval of 0.19 eV.

In addition a much weaker series of progressions arises from modes $\nu_{eff,2}$ to $\nu_{eff,5}$, involving collective stretching, deformation and rocking of the ligand rings (see more details in Figures S36, S37 and S38).

The last contribution to the emission spectrum, mostly by increasing the second peak intensity, is a low-frequency mode ($\nu_{eff,6}$= 46 cm^{-1}) responsible for the rocking of the entire ligands.

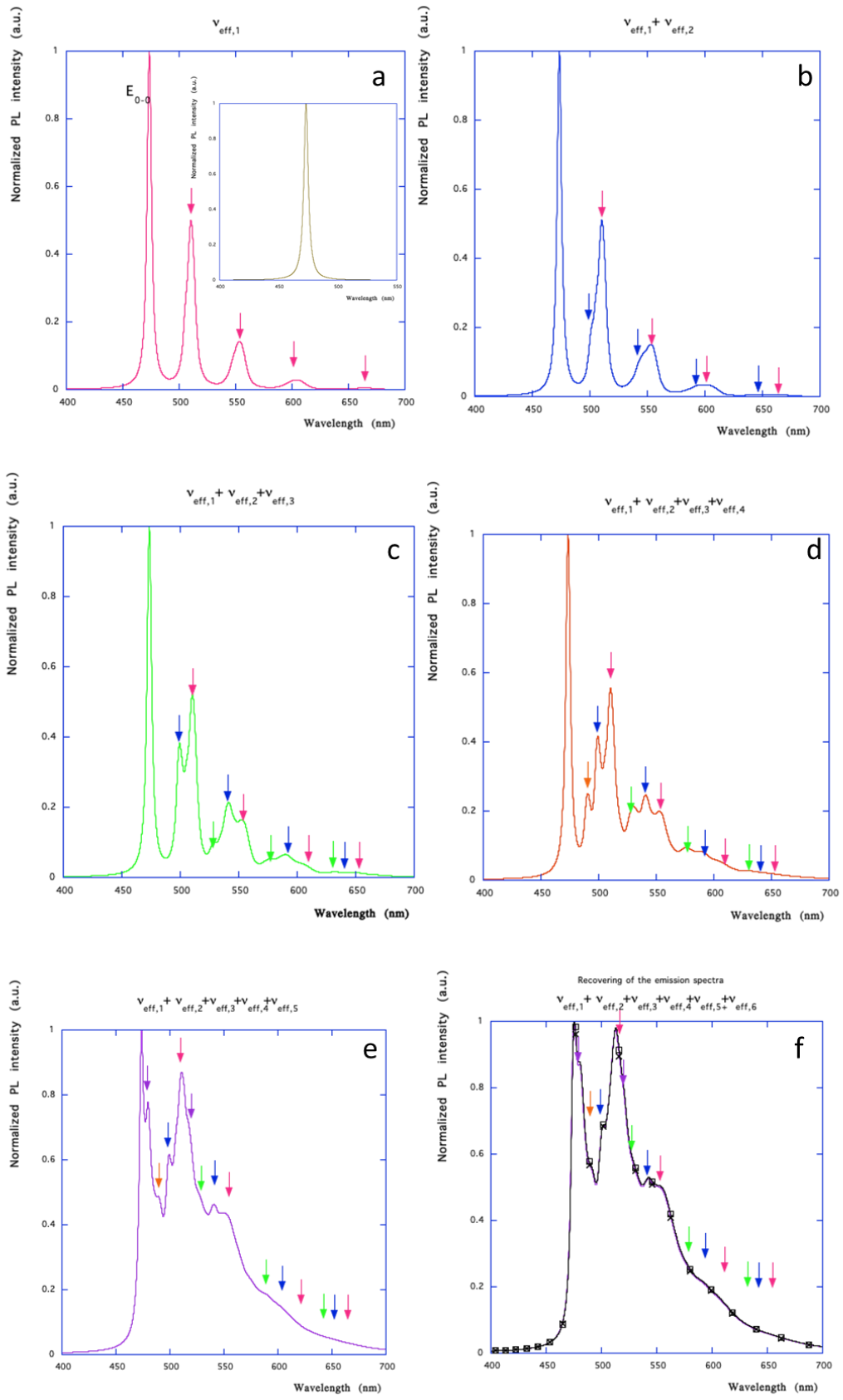

Figure S36. Step by step procedure for the identification of effective frequencies numbered from 1 to 6. Each contribution is spotted by different colored arrows.

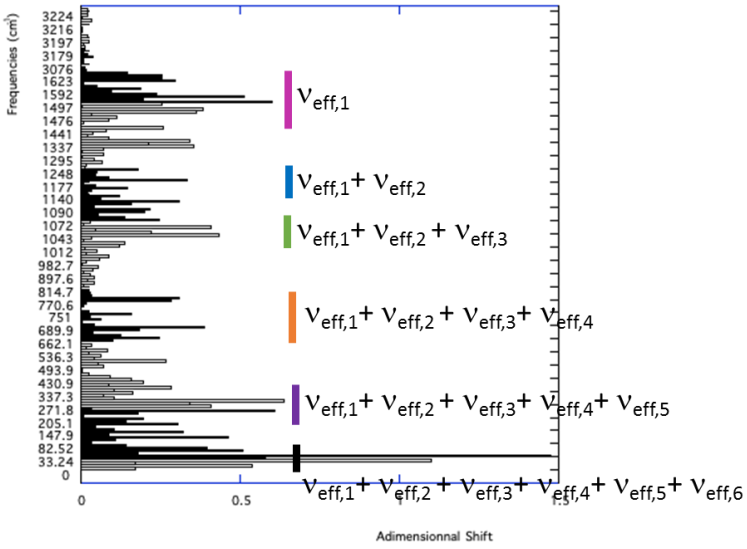

$\nu_{eff,1}$: 1648, 1626, 1622, 1609, 1590, 1514 cm-1 = C-C and C-N stretching + In-plane hydrogen wagging motions

$\nu_{eff,2}$: 1266, 1181, 1135cm^{-1}: = C-C and C-N stretching+ In-plane hydrogen wagging motions+ Valence deformations(CCH,CCN)

$\nu_{eff,3}$: 1097, 1063, 1061, 1054cm^{-1} : = C-C and C-N stretching + Out of plane aromatic hydrogen wagging motions+ Valence deformations(CCH,CCN)

$\nu_{eff,4}$: 783, 782, 695, 519 cm^{-1}:Valence deformations(CCH,CCN)+ Ir-C (slight contribution) +Ir-N(slight contribution)

$\nu_{eff,5}$: 285, 188, 135cm^{-1}: Ring Rocking

$\nu_{eff,6}$: 46 cm^{-1}: Rocking of the entire ligand

Figure S37. Adimensional displacements and their associated frequencies. Color code is the same as in Figure S36.

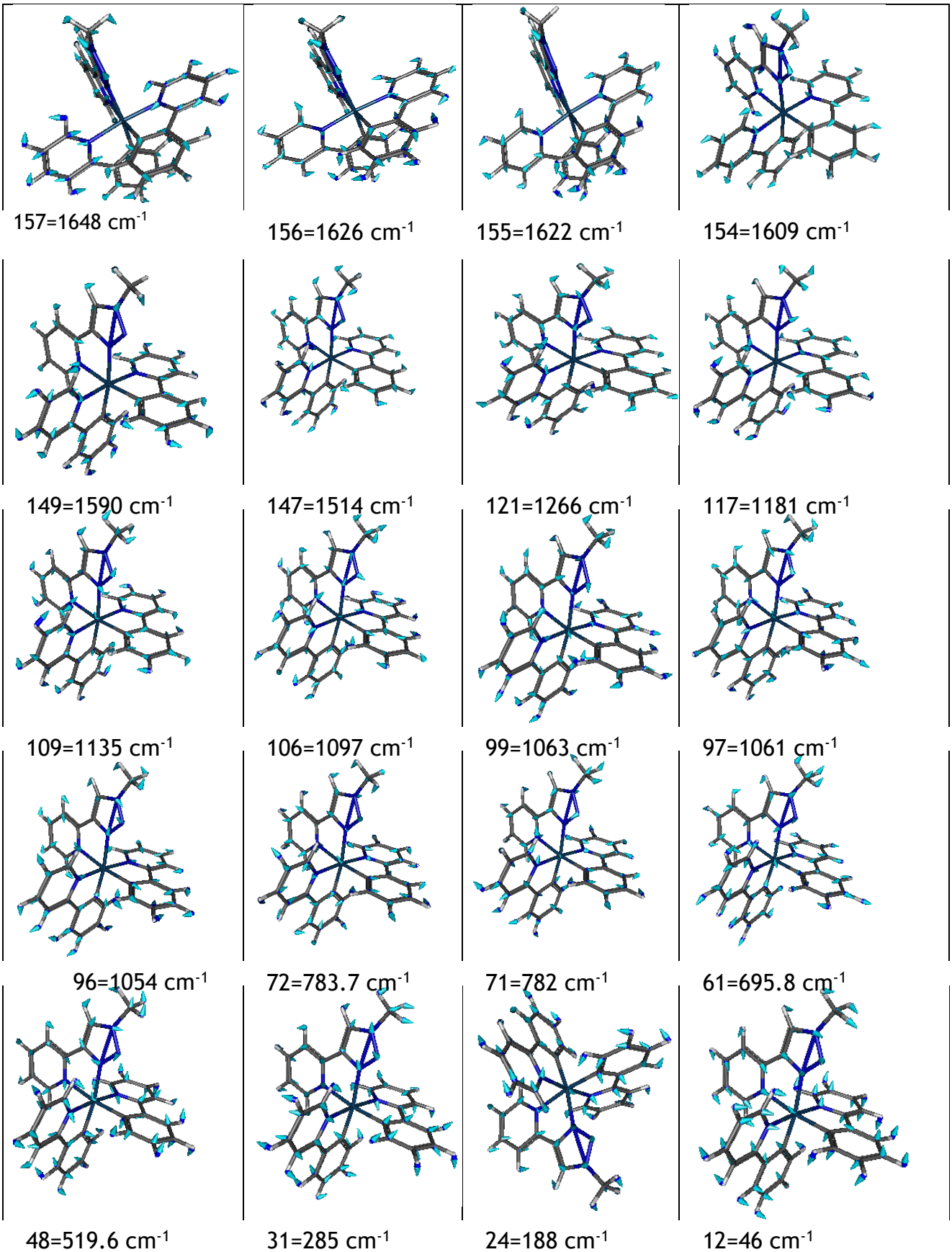

Figure S38. Representation of the atomic displacements involved in the modes responsible for the multi-peak emission spectrum of ^{3}MLCT/^{3}LC of **1a**.

Theoretical analysis of the vibrational resolved emission spectrum of the ^{3}MLCT/^{3}LL'CT state of compound 1b.

By reducing the line broadening factors, we can favor the appearance of the fine structure and discuss of the vibronic progressions even though it not visible on experimental spectra.

This spectrum is easier to analyze than the previous one (e.g. **1a**), as very few vibrational modes dominate the emission spectrum of **1b**. Consequently the strategy to identify the vibrational mode responsible for the structure was different. We removed from the calculation all modes with a large ddnc (see Figure S39). In case the resulting spectrum is affected, this is a strong indication of the importance of this mode in the structuration. The results of these protocol is presented on Figure S39. The main contribution is due to a combination of modes 132-134, the maximum wavelength coinciding with the 0→1 transition. These modes are localized solely on a unique ligand i.e the ancillary ligand, contrary to what is observed in the ^{3}LC case. They correspond to in-plane C-Haromatic wagging and C-C stretching (see Figure S40). The intense contribution localised at large wavelength, near 640 nm, is due to mode 158 and corresponds to a high-frequency vibration (3080 cm^{-1}) involving methyl CH stretching (Figure S40). This is clearly a drawback of our model, Bn being replaced by Me, and might explain the less impressive agreement between theory and experiment for the ^{3}LL'CT case.

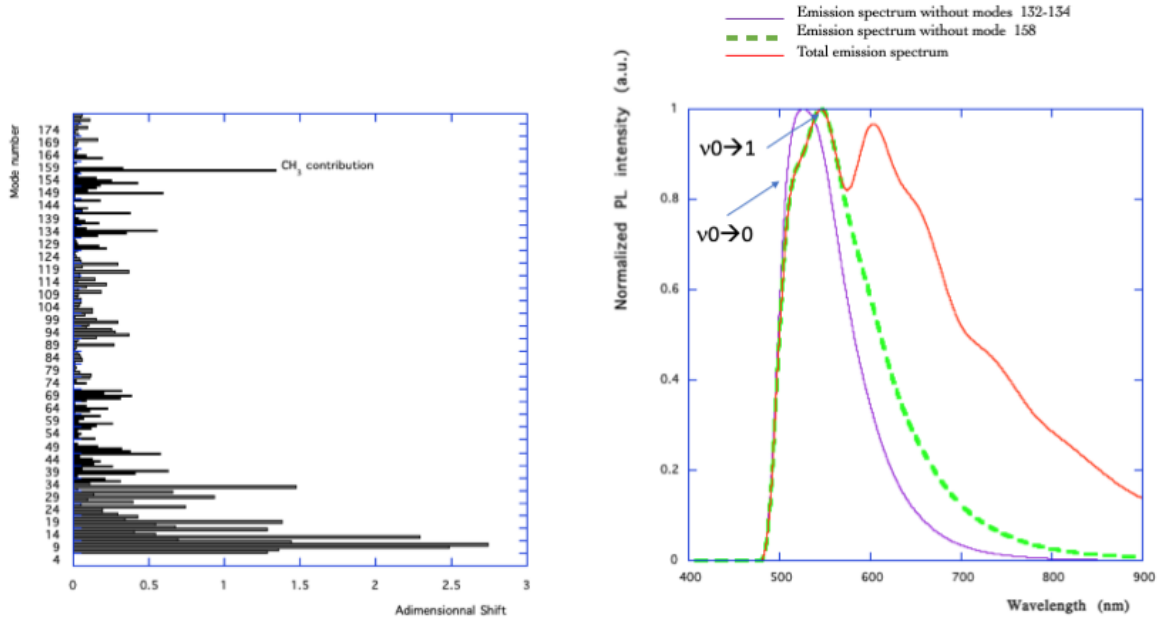

Figure S39. On the left adimensional displacements, DDNC, for each vibrational mode of the ^{3}MLCT/^{3}LL'CT state of **1b**. On the right VRES of ^{3}MLCT/^{3}LL'CT in red, VRES without the CH of CH_3 stretching in green and VRES without modes 132-134 in purple.

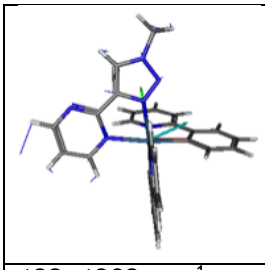	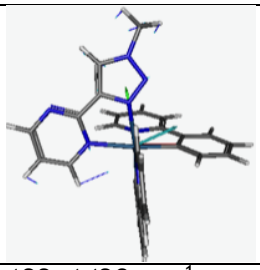	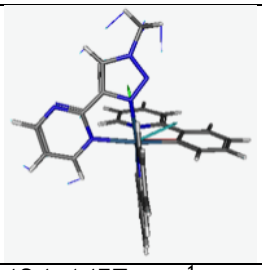	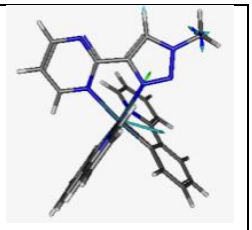
132=1393 cm^{-1}	133=1438 cm^{-1}	134=1457 cm^{-1}	158=3080 cm^{-1}

Figure S40. Representation of the atomic displacements involved in the modes responsible for the emission spectrum of ^{3}MLCT/^{3}LL'CT of **1b**.

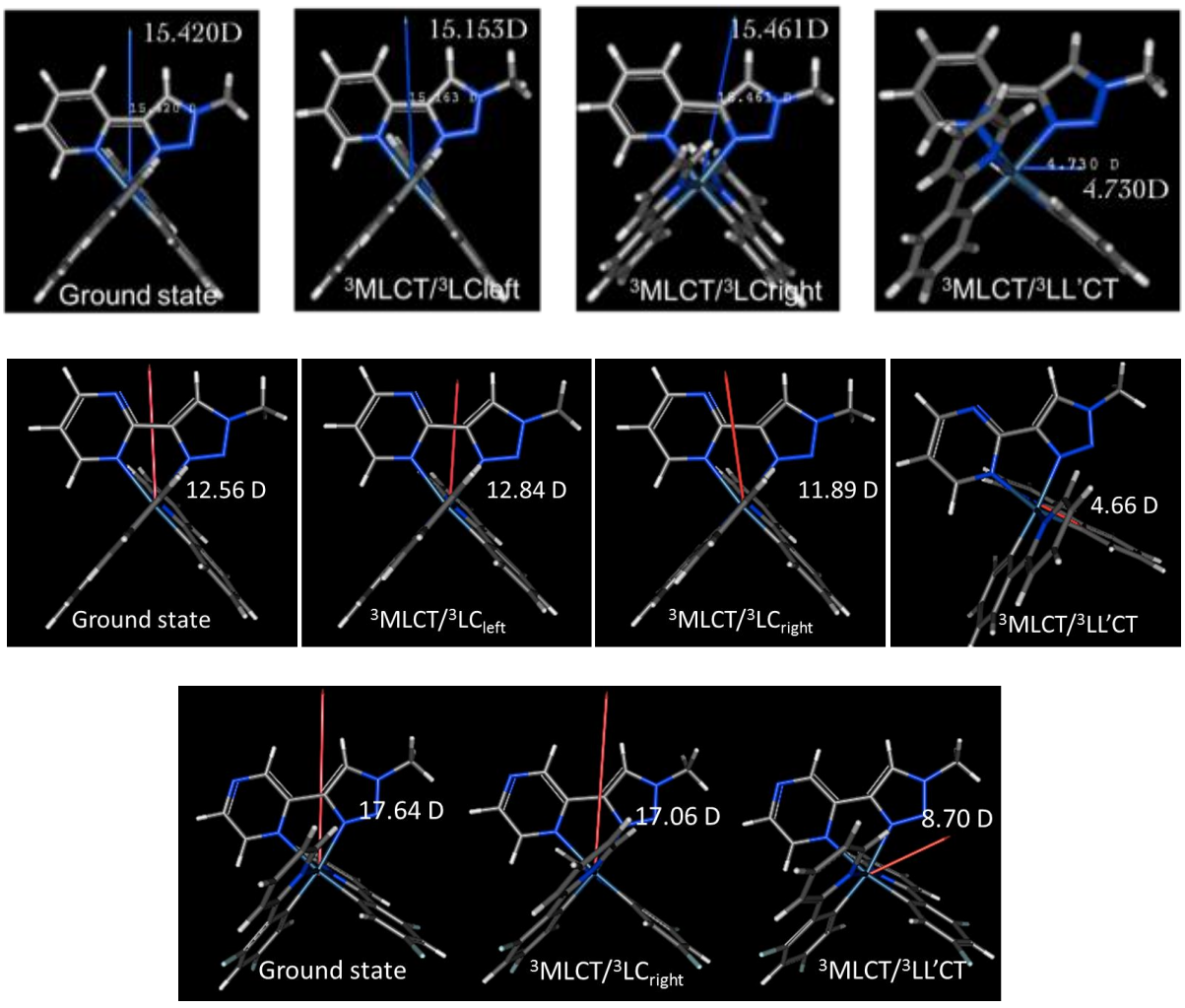

Figure S41. Dipole moments of **1a** (top), **1b** (middle) and **2c** (bottom) in their ground state and lowest triplet states calculated in MeCN using SMD model. Arrows represent the orientation of the dipole and the magnitude is in Debye.

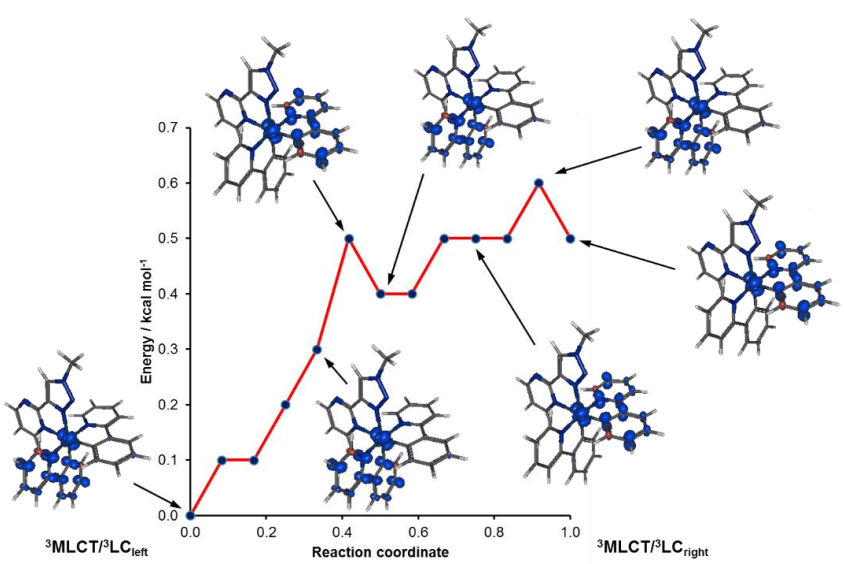

Figure S42. Spin density plots and T_1 PES minimum energy path between the ^{3}MLCT/^{3}LC$_{left}$ and ^{3}MLCT/^{3}LC$_{right}$ states for **1b** from a nudged elastic band optimisation calculation in MeCN using SMD model.

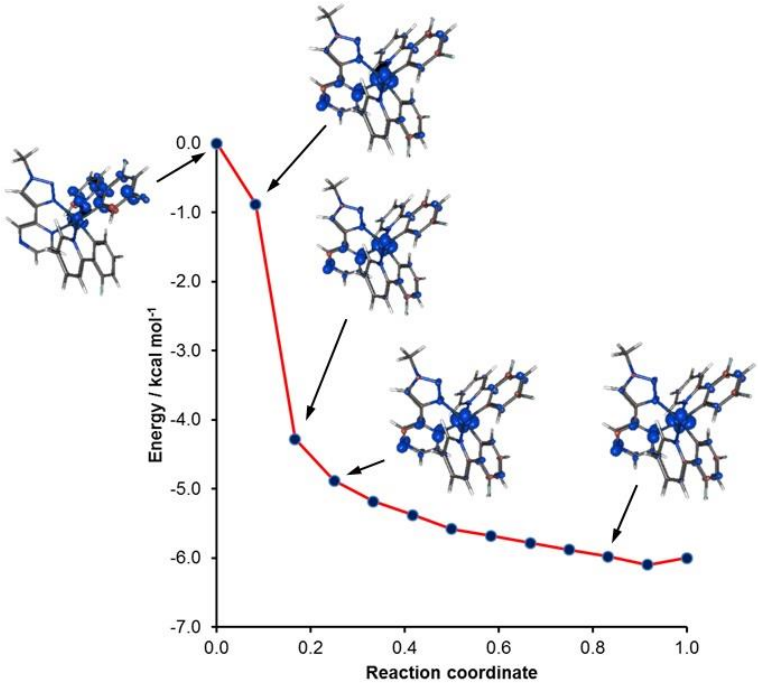

Figure S43. Spin density plots and T_1 PES minimum energy path between the ^{3}MLCT/^{3}LC state and ^{3}MLCT/^{3}LL'CT state for **2c** from a nudged elastic band optimisation calculation in MeCN using SMD model.

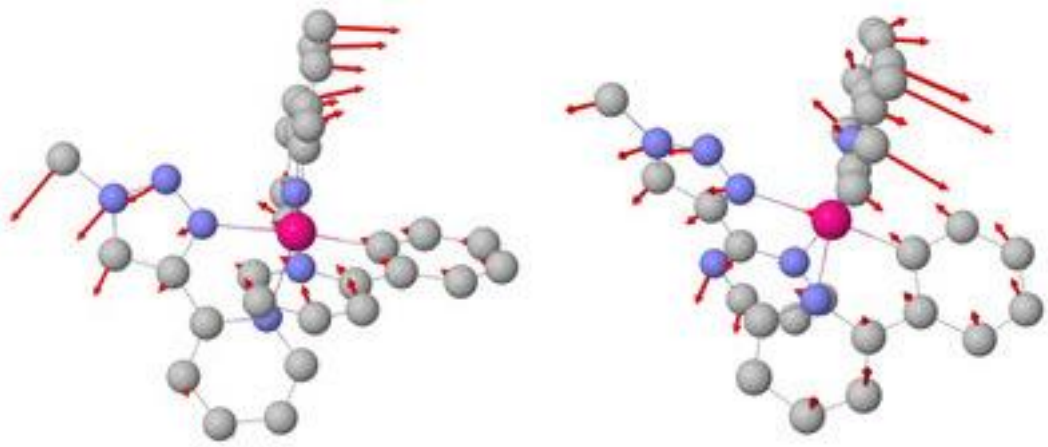

Figure S44. Transition state mode at the highest energy point along the ^{3}MLCT/^{3}LL'CT - ^{3}MLCT/^{3}LC$_{left}$ minimum energy paths for **1a** (left) and **1b** (right) in MeCN using SMD model.

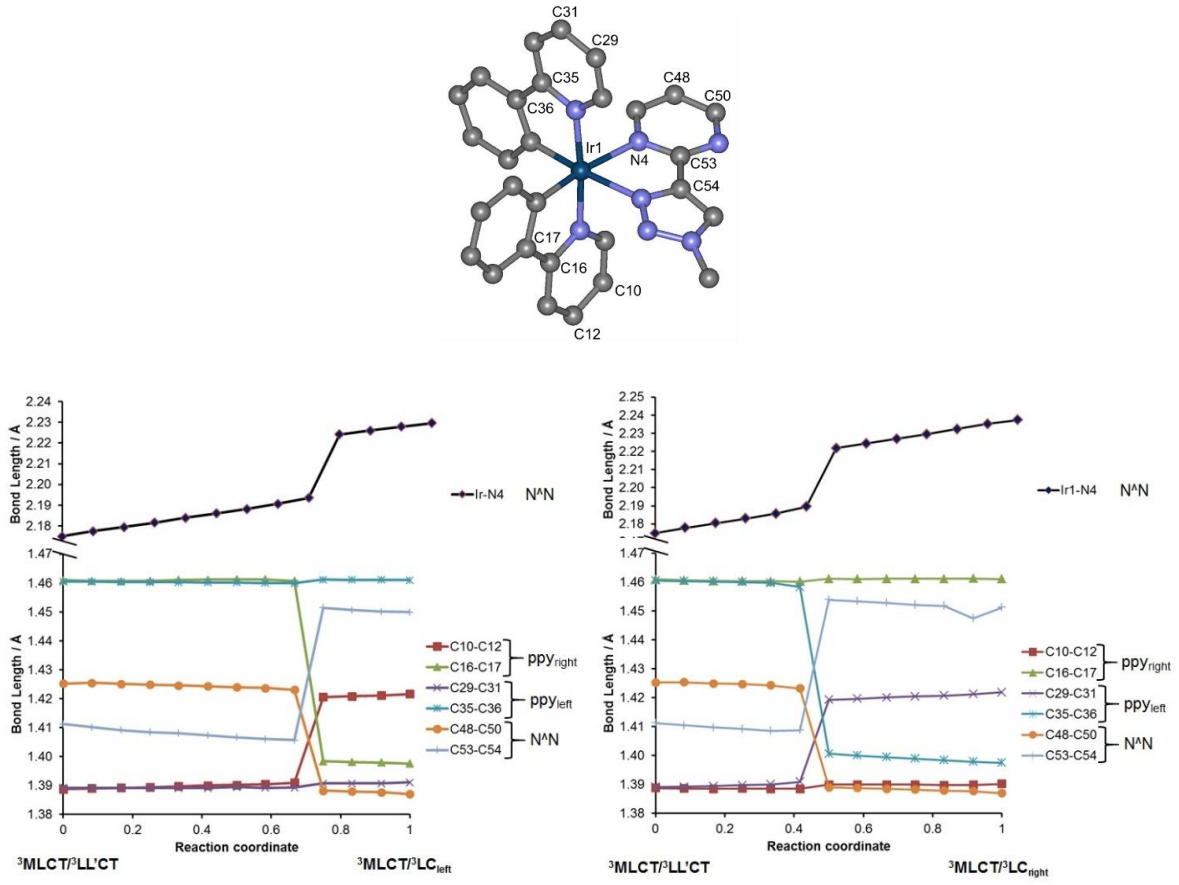

Figure S45. Evolution of selected bond lengths for **1b** along minimum energy paths from NEB calculations - in MeCN using SMD model - connecting the ^{3}MLCT/^{3}LL'CT state to the ^{3}MLCT/^{3}LC$_{left}$ and ^{3}MLCT/^{3}LC$_{right}$ states.

References

1. M. Nonoyama, *Bulletin of the Chemical Society of Japan*, 1974, **47**, 767-768.
2. E. Baranoff, B. F. E. Curchod, F. Monti, F. Steimer, G. Accorsi, I. Tavernelli, U. Rothlisberger, R. Scopelliti, M. Grätzel and M. K. Nazeeruddin, *Inorganic Chemistry*, 2012, **51**, 799-811.
3. M. Obata, A. Kitamura, A. Mori, C. Kameyama, J. A. Czaplewska, R. Tanaka, I. Kinoshita, T. Kusumoto, H. Hashimoto, M. Harada, Y. Mikata, T. Funabiki and S. Yano, *Dalton Transactions*, 2008, DOI: 10.1039/B718538C, 3292-3300.
4. T. U. Connell, J. M. White, T. A. Smith and P. S. Donnelly, *Inorganic Chemistry*, 2016, **55**, 2776-2790.
5. M. Mydlak, C. Bizzarri, D. Hartmann, W. Sarfert, G. Schmid and L. De Cola, *Advanced Functional Materials*, 2010, **20**, 1812-1820.
6. B. S. Uppal, R. K. Booth, N. Ali, C. Lockwood, C. R. Rice and P. I. P. Elliott, *Dalton Transactions*, 2011, **40**, 7610-7616.
7. K. K. W. Lo, K. Y. Zhang, S. K. Leung and M. C. Tang, *Angewandte Chemie - International Edition*, 2008, **47**, 2213-2216.
8. G. M. Sheldrick.
9. F. Neese, *Wiley Interdisciplinary Reviews: Computational Molecular Science*, 2012, **2**, 73-78.
10. F. Neese, *Wiley Interdisciplinary Reviews: Computational Molecular Science*, 2018, **8**, e1327.
11. A. D. Becke, *The Journal of Chemical Physics*, 1993, **98**, 1372-1377.
12. C. Lee, W. Yang and R. G. Parr, *Physical Review B*, 1988, **37**, 785-789.
13. S. Grimme, J. Antony, S. Ehrlich and H. Krieg, *Journal of Chemical Physics*, 2010, **132**.
14. S. Grimme, S. Ehrlich and L. Goerigk, *Journal of Computational Chemistry*, 2011, **32**, 1456-1465.
15. F. Weigend and R. Ahlrichs, *Physical Chemistry Chemical Physics*, 2005, **7**, 3297-3305.
16. X. Zhou, P. L. Burn and B. J. Powell, *Inorganic Chemistry*, 2016, **55**, 5266-5273.
17. X. Zhou and B. J. Powell, *Inorganic Chemistry*, 2018, **57**, 8881-8889.
18. A. V. Marenich, C. J. Cramer and D. G. Truhlar, *Journal of Physical Chemistry B*, 2009, **113**, 6378-6396.
19. G. Henkelman, G. Jóhannesson and H. Jónsson, *Progress in Theoretical Chemistry and Physics*, 2000, **5**, 269-300.
20. H. Jónsson, G. Mills and K. W. Jacobsen, *Classical and Quantum Dynamics in Condensed Phase Simulations*, 1998.
21. H. C. Herbol, J. Stevenson and P. Clancy, *Journal of Chemical Theory and Computation*, 2017, **13**, 3250-3259.
22. S. Smidstrup, A. Pedersen, K. Stokbro and H. Jónsson, *Journal of Chemical Physics*, 2014, **140**.
23. T. Petrenko and F. Neese, Journal of Chemical Physics 2007, **127**, 164319.
24. M. de Jong, L. Seijo, A. Meijerink and F.T. Rabouw, Physical Chemistry Chemical Physics, 2015, **17**, 16959-16969.
25. J. Guo, X. Pan, X. Wang, W. Wu and J. Zhang, *Organic Electronics*, 2018, **61**, 125-133.